
Align & Invert: Solving Inverse Problems with Diffusion and Flow-based Models via Representation Alignment

Loukas Sfountouris¹ Giannis Daras² Paris Giampouras¹

Abstract

Enforcing alignment between the internal representations of diffusion or flow-based generative models and those of pretrained self-supervised encoders has recently been shown to provide a powerful inductive bias, improving both convergence and sample quality. In this work, we extend this idea to inverse problems, where pretrained generative models are employed as *priors*. We propose applying *representation alignment* (REPA) between diffusion or flow-based models and a DINOv2 visual encoder, to guide the reconstruction process at inference time. Although ground-truth signals are unavailable in inverse problems, we empirically show that aligning model representations of approximate target features can substantially enhance reconstruction quality and perceptual realism. We provide theoretical results showing (a) that REPA regularization can be viewed as a variational approach for minimizing a divergence measure in the DINOv2 embedding space, and (b) how under certain regularity assumptions REPA updates steer the latent diffusion states toward those of the clean image. We integrate REPA into multiple state-of-the-art inverse problem solvers, and provide extensive experiments on super-resolution, box inpainting, Gaussian deblurring, and motion deblurring confirming that our method consistently improves reconstruction quality, while also providing efficiency gains reducing the number of required discretization steps.

1. Introduction

Pretrained diffusion and flow-based models, (Sohl-Dickstein et al., 2015; Ho et al., 2020; Esser et al., 2024; Lipman et al., 2023), have recently been at the heart of methods focusing

¹Department of Computer Science, University of Warwick, Coventry, England ²Massachusetts Institute of Technology, Massachusetts, USA. Correspondence to: Loukas Sfountouris <loukas.sfountouris@warwick.ac.uk>.

on addressing various types of inverse problems. The crux of these approaches is to perform diffusion sampling, incorporating measurement information during the reverse process, with the goal to reconstruct the clean image at the final step, (Patel et al., 2024; Chung et al., 2023; Thaker et al., 2025). Undoubtedly, diffusion and flow-based models have pushed the boundaries in addressing a wealth of inverse problems, (Daras et al., 2024). However, they still struggle to produce highly detailed images particularly in cases of severe degradation and in challenging scenes, such as natural images with rich textures and complex backgrounds. These issues are further exacerbated when using latent diffusion models (Rombach et al., 2022), where the inclusion of encoder-decoder architectures introduces additional challenges during the reverse process due to nonlinearities. To mitigate these limitations, further inductive biases are needed during inference, (Rout et al., 2023; Raphaeli et al., 2025).

Recent studies have shown that diffusion models learn semantic features in their hidden states, (Li et al., 2023). The more expressive these features are the better the diffusion model performs on the generative task, (Xiang et al., 2023). Building on this insight, the seminal work of Yu et al. (2024) introduced a regularizer that aligns the internal representations of the diffusion model with those of a pretrained visual encoder, (Oquab et al., 2023). This framework, termed *representation alignment* (REPA), was shown to act as a strong semantic constraint leading to higher-fidelity generations and significantly faster convergence.

The success of REPA has attracted considerable interest in this direction, (Wang et al., 2025b; Tian et al., 2025; Yao et al., 2025; Leng et al., 2025; Wang et al., 2025a). In particular, (Wang et al., 2025b) observed that while REPA enhances early training dynamics, its benefits diminish over time and can even degrade performance in later iterations. To address this issue, they introduced an early-stopping strategy which mitigated the late-stage degradation and further improved overall convergence speed. Other works have explored applying alignment losses directly to VAE latent spaces (Yao et al., 2025; Xu et al., 2025), finding that diffusion models trained on these regularized spaces converge faster. Despite these advances, most efforts focus on improving training efficiency, whereas relatively little attention

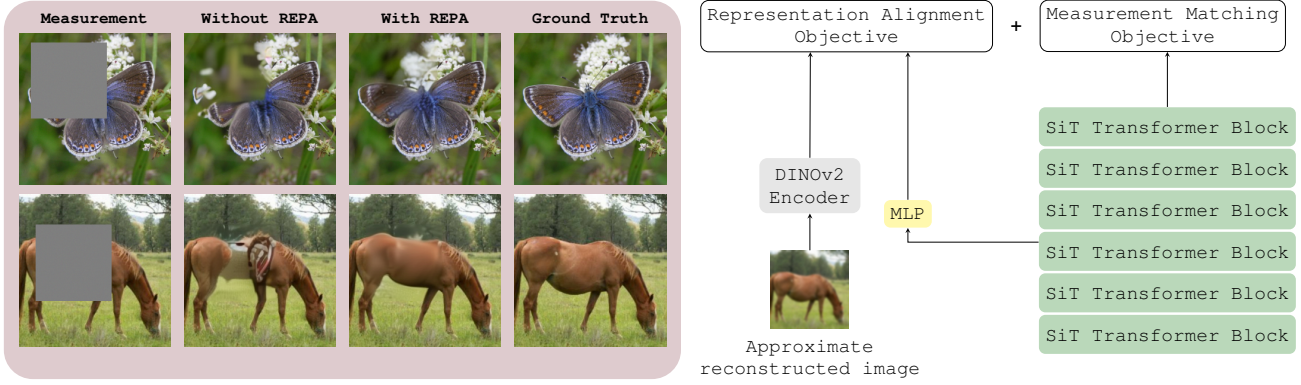


Figure 1. Overview of our proposed framework. Left: Box inpainting (top row) and Gaussian deblurring (bottom row) results, where adding REPA improves perceptual quality. Right: Alignment between diffusion features and pretrained DINOv2 embeddings.

has been paid to leveraging representation alignment at inference time, particularly for solving inverse problems. This motivates our central question:

Can we apply representation alignment to benefit existing algorithms for solving inverse problems using pretrained diffusion and flow-based models?

Contributions. Our main contributions are as follows:

- We introduce a general framework for solving inverse problems with diffusion and flow-based models by enforcing alignment between internal diffusion representations and DINOv2 features (Fig. 1). Despite the absence of ground truth, alignment with proxy reconstructions remains effective thanks to the robustness/invariances of DINOv2 representations.
- We provide theoretical results that characterize the effect of the REPA regularizer: (a) its connection to a divergence measure defined in the DINOv2 feature space, and (b) under suitable regularity assumptions, its ability to steer latent diffusion states toward those associated with the clean image.
- We demonstrate the versatility of our approach by integrating representational alignment into different existing state-of-the-art inverse problem solvers.
- Through extensive experiments on super-resolution, Gaussian deblurring, motion deblurring, and box inpainting, we show consistent improvements over prior methods across tasks and metrics, and further demonstrate that applying REPA to existing solvers allows them to match their original performance using significantly fewer discretization steps.

2. Related Work

2.1. Diffusion & Flow-based Models

Generative models based on denoising are a class of deep generative models that aim to learn a data distribution $p_0(x)$ by training on progressively corrupted versions of real sam-

ples (Sohl-Dickstein et al., 2015; Ho et al., 2020; Song et al., 2021; Liu et al., 2023). These models define a) a forward (noising) process, which gradually interpolates between the data distribution and a reference distribution $p_1(x)$ (typically a Gaussian), and b) a reverse (denoising) process, which is trained to invert this corruption and iteratively reconstruct data from noise. Following the formulation of stochastic interpolants (Albergo et al., 2023), the time marginals of this process can be expressed as

$$x_t = \alpha_t x^* + \sigma_t \varepsilon, \quad x^* \sim p_0(x), \quad \varepsilon \sim \mathcal{N}(0, I), \quad (1)$$

where α_t and σ_t correspond to decreasing and increasing function of t , respectively, with boundary conditions $\alpha_0 = \sigma_1 = 1$ and $\alpha_1 = \sigma_0 = 0$. Throughout, we use the notation $\dot{\alpha}_t := \frac{d\alpha_t}{dt}$ and $\dot{\sigma}_t := \frac{d\sigma_t}{dt}$ to denote time derivatives. Lipman et al. (2023) showed that there exists a probability flow ordinary differential equation (ODE) whose solution follows the same time marginals as the process in eq. (1):

$$\dot{x}_t = v(x_t, t), \quad (2)$$

where $v(x_t, t)$ denotes the true drift field that transports $p_0(x)$ to $p_1(x)$. To enable sampling from the data distribution, one has to train a neural network $v_\theta(x_t, t)$ to approximate $v(x_t, t)$. This is done by regressing the network output toward the optimal vector field using *conditional flow matching* (Lipman et al., 2023; Hyvärinen & Dayan, 2005), minimizing

$$\mathcal{L}_{\text{velocity}}(\theta) := \mathbb{E}_{x^*, \varepsilon, t} [\|v_\theta(x_t, t) - \dot{\alpha}_t x^* - \dot{\sigma}_t \varepsilon\|^2], \quad (3)$$

Beyond the ODE view, there also exists a reverse *stochastic differential equation* (SDE) with the same time marginals:

$$dx_t = v(x_t, t) dt - g^2(t) s(x_t, t) dt + g(t) d\bar{w}_t, \quad (4)$$

where $s(x_t, t) = \nabla_{x_t} \log p_t(x_t)$ is the score, $g(t)$ is the diffusion coefficient, and \bar{w}_t is a standard Wiener process

running backward in time. Notably, the score can be expressed directly in terms of the velocity field:

$$s(x_t, t) = \sigma_t^{-1} \cdot \frac{\alpha_t v(x_t, t) - \dot{\alpha}_t x_t}{\dot{\alpha}_t \sigma_t - \alpha_t \dot{\sigma}_t}. \quad (5)$$

Eq. (5) hints that the score parameterization used in diffusion models and the velocity parameterization used in flow-based models can lead to equivalent formulations of the sampling process. In practice, diffusion models correspond to a stochastic discretization of the probability flow ODE, while flow-based models correspond to its deterministic counterpart (Lai et al., 2025).

2.2. Diffusion Models with Representation Guidance

Diffusion models learn rich, discriminative features in their hidden states, which are crucial for their generative performance (Xiang et al., 2023). Nevertheless, their learned representations still fall behind on downstream tasks when compared with state-of-the-art self-supervised visual encoders, (Assran et al., 2023; Siméoni et al., 2025). This representation gap has been identified as a key bottleneck for improving the generative performance of diffusion models, as richer and more semantically structured representations have been shown to enhance sample fidelity (Yu et al., 2024). To address this, a growing line of work introduces representation guidance, which conditions diffusion models on external representations from pretrained self-supervised encoders (Li et al., 2024). Typically these approaches fall into two categories: (i) conditioning the diffusion model on external representations, either learned, (Li et al., 2024), or retrieved from a database of samples, (Blattmann et al., 2022; Hu et al., 2023; Sheynin et al., 2022); and (ii) explicitly aligning the model’s internal representations with those of large pretrained encoders, thereby encouraging more semantically meaningful feature-spaces, (Tian et al., 2025; Hu et al., 2023; Leng et al., 2025).

Within the REPA framework, feature-level alignment is applied directly to intermediate representations of the diffusion model. In particular, let the diffusion model consist of L transformer blocks, and $\ell \in \{1, \dots, L\}$ denote the layer at which features are extracted. The quantity $h_t \in \mathbb{R}^{N \times D_2}$ denotes the matrix of patch tokens obtained after the first ℓ transformer blocks when the model processes an input image x at timestep t . Here, N is the number of patch tokens and D_2 the embedding dimension, with $h_t^{[n]} \in \mathbb{R}^{D_2}$ representing the n -th patch token. For convenience, this is written as

$$h_t = \text{DIFFENC}(x_t, t),$$

where x_t denotes the noisy image and `DIFFENC` returns the patch-level hidden representation after the first ℓ blocks of the diffusion model’s transformer encoder. REPA enforces patch-wise similarity between the D_1 -dimensional DINOv2

representation of the target image x , i.e., $f_{\text{DINOv2}}^{[n]}(x) \in \mathbb{R}^{D_1}$ for patches $n = 1, \dots, N$, and the intermediate hidden states $h_t^{[n]}$, by maximizing the following objective during training:

$$\text{REPA}(x, h_t) = \frac{1}{N} \sum_{n=1}^N \cos\left(f_{\text{DINOv2}}^{[n]}(x), g_\phi(h_t^{[n]})\right), \quad (6)$$

where $g_\phi : \mathbb{R}^{D_2} \rightarrow \mathbb{R}^{D_1}$ is a learnable multi-layer perceptron (MLP) that projects hidden states into the DINOv2 embedding space. By jointly optimizing $\mathcal{L}_{\text{REPA}}$ with the standard diffusion loss, the model learns internal representations that are semantically richer and better aligned with high-level visual features, ultimately yielding higher-quality image generation and faster convergence during training.

2.3. Inverse Problems with Diffusion and Flow Models

When solving inverse problems the goal is to recover the clean signal x_0 from noisy or degraded measurements y . In the flow- and diffusion-based framework, this is accomplished by replacing the unconditional score function in eq. (4) with the conditional score $\nabla_{x_t} \log p(x_t | y)$. Applying Bayes’ rule, the conditional score can be decomposed as

$$\nabla_{x_t} \log p(x_t | y) = \nabla_{x_t} \log p_t(x_t) + \nabla_{x_t} \log p(y | x_t),$$

Using this decomposition, the reverse-time SDE becomes

$$dx_t = (v(x_t, t) - g^2(t) \nabla_{x_t} \log p(x_t | y)) dt + g(t) d\bar{w}_t.$$

The unconditional score $\nabla_{x_t} \log p_t(x_t)$ is provided by a pretrained diffusion or flow-based model, while the likelihood term $\nabla_{x_t} \log p(y | x_t)$ enforces measurement consistency but is generally intractable, as it requires marginalizing over all possible clean signals x_0 . One of the most prominent approaches is *Diffusion Posterior Sampling (DPS)*, (Chung et al., 2023), which uses the following approximation:

$$p(y | x_t) \approx p(y | \hat{x}_0 = \mathbb{E}[x_0 | x_t]),$$

where $\mathbb{E}[x_0 | x_t]$ denotes the conditional expectation of x_0 given x_t . In many practical scenarios, performing the diffusion process directly in pixel space is computationally prohibitive. Latent diffusion models (LDMs) address this limitation by operating in a compressed latent space. Let $\mathcal{E} : \mathbb{R}^k \rightarrow \mathbb{R}^d$ be an encoder mapping an image x_0 to its latent representation $z_0 = \mathcal{E}(x_0)$, and let \mathcal{D} denote the corresponding decoder such that $\hat{x}_0 = \mathcal{D}(z_0) \approx x_0$. Building on this formulation, recent work has proposed latent-space counterparts of pixel-based inverse problem solvers. For example, Diffusion Posterior Sampling (DPS) has been formulated in latent space by redefining the measurement likelihood as

$$p(y | z_t) \approx p(y | \hat{x}_0 = \mathcal{D}(\mathbb{E}[z_0 | z_t])).$$

This straightforward formulation commonly referred to as Latent DPS has been observed to introduce artifacts, largely due to the nonlinearity of the decoder. To mitigate this effect, Rout et al. (2023) proposed a regularization term encouraging the latent variables to remain close to a fixed point of the encoder–decoder mapping, while Song et al. (2024) enforced data consistency during optimization followed by a projection of the latent variables back onto the noisy manifold.

3. Proposed Approach

Given a noisy observation $y \in \mathbb{R}^m$ of an unknown signal $x \in \mathbb{R}^k$, our goal is to sample from $p_\theta(x_0 | y)$ using a pretrained diffusion- or flow-based model.

We aim to apply REPA framework to inverse problems. However, a key challenge is that representation alignment requires access to the ground-truth signal, which is not available in this setting. To overcome this, we must choose an alternative input to the DINOv2 encoder that can stand in for the missing ground truth. In particular, we need an approximation \bar{x}_0 of the unknown x_0 that produces a *proxy representation* $c_{\text{proxy}} \in \mathbb{R}^{N \times D_1}$, where N denotes the number of patch tokens and D_1 is their feature dimension. This representation should satisfy

$$c_{\text{proxy}} \equiv f_{\text{DINOv2}}(\bar{x}_0) \approx f_{\text{DINOv2}}(x_0). \quad (7)$$

We then introduce a *tilted distribution*, (Pachebat et al., 2025), that incorporates representation alignment as an additional reward:

$$\tilde{p}(x_t | y) \propto p(y | x_t) p_t(x_t) \exp(\lambda \text{REPA}(\bar{x}_0, h_t)), \quad (8)$$

where $h_t = \text{DIFFENC}(x_t, t)$ denotes the intermediate diffusion representation and $\lambda > 0$ controls the strength of the alignment term. The likelihood $p(y | x_t)$ enforces measurement consistency, while $p_t(x_t)$ corresponds to the unconditional prior induced by the pretrained diffusion or flow model. The REPA term is defined in Eq. (6) and encourages alignment between the diffusion representation of x_t and the proxy DINOv2 features c_{proxy} , thereby biasing the sampling process toward semantically consistent reconstructions.

On the selection of c_{proxy} . To address the fact that representation alignment (Yu et al., 2024) is not directly applicable to inverse problems where the ground-truth image is unavailable at inference time, we construct c_{proxy} from an approximate reconstruction. We initialize the proxy using the DINOv2 features of the available observation and, as the reverse diffusion process progresses and the reconstruction becomes more informative, we gradually replace this proxy with the features of the model’s current denoised estimate, namely $f_{\text{DINOv2}}(\mathbb{E}[x_0 | x_t])$. In both cases, we rely on the

robustness of pretrained DINOv2 features, which, as shown in our experiments, remain stable under the degradations present in super-resolution and deblurring tasks. An ablation in Appendix A.4 quantifies the reliability of this proxy across tasks.

Extension to latent diffusion models. The proposed representation-alignment strategy applies naturally to latent diffusion models, where sampling is performed in a learned latent space rather than in pixel space. Let z_t denote the latent state at timestep t . In this setting, the tilted distribution becomes

$$\tilde{p}(z_t | y) \propto p(y | z_t) p_t(z_t) \exp(\lambda \text{REPA}(\bar{x}_0, h_t)),$$

With a slight abuse of notation, we use DIFFENC to denote the diffusion encoder in both pixel-space and latent-space models, and write $h_t = \text{DIFFENC}(z_t, t)$ for latent diffusion.

Our general algorithm for a latent-space velocity-based sampler is summarized in Algorithm 1. Step 6 is intentionally kept abstract; as discussed in Section 2.3, different inverse-problem solvers approximate this term in different ways. The proposed regularizer is compatible with standard diffusion-based reconstruction pipelines. In our experiments, we instantiate the framework using two state-of-the-art latent diffusion methods, with further implementation details provided in Appendix A.2 and Appendix A.3.

Algorithm 1 REPA-regularized Inverse Algorithm

Require: Flow or diffusion model u_θ , measurement y , learning rate η , regularizer strength λ , proxy representation c_{proxy} , timestep t_{cutoff} , Decoder \mathcal{D}

- 1: Initialize $z_T \sim \mathcal{N}(0, I)$,
- 2: **for** $t = T, \dots, 1$ **do**
- 3: $v \leftarrow u_\theta(z_t, t)$
- 4: $\Delta t \leftarrow 1/T$
- 5: $z_{t-1} \leftarrow z_t - \Delta t \cdot v$
- 6: $z_{t-1} \leftarrow z_{t-1} + \eta \nabla_{z_t} \log p(y | z_t)$
- 7: $z_{t-1} \leftarrow z_{t-1} + \lambda \nabla_{z_t} \sum_{n=1}^N \cos(c_{\text{proxy}}^{[n]}, g_\phi(\text{DiffEnc}^{[n]}(z_t, t)))$
- 8: **if** $t < t_{\text{cutoff}}$ **then**
- 9: $c_{\text{proxy}} \leftarrow f_{\text{DINOv2}}(\mathcal{D}(\mathbb{E}[z_0 | x_t]))$
- 10: **end if**
- 11: **end for**
- 12: **return** z_0

4. Theoretical Results

Recent advances in generative modeling have demonstrated that objectives defined in deep feature spaces, rather than purely pixel-based discrepancies, produce reconstructions that better capture perceptual similarity (Dosovitskiy & Brox, 2016; Zhang et al., 2018; Fu et al., 2023). Motivated

by this observation, our goal in this section is to clarify how the REPA regularizer fits within this broader class of feature-based objectives. In particular, we present two theoretical results that characterize how REPA acts on (i) the DINOv2-space representations of reconstructed images and (ii) the latent diffusion state itself.

First, we show that the REPA term can be viewed as an empirical surrogate for minimizing a feature-space divergence specifically, the maximum mean discrepancy (MMD) between the DINOv2 features of reconstructed images and those of the ground truth. Second, we study how REPA affects the latent states of the diffusion model during the reverse process. Under suitable assumptions, we show that a REPA update moves the current diffusion state toward the latent representation of the clean image. This provides a complementary view: REPA influences not only the DINOv2 representation of the reconstruction but also the latent state that guides the sampling trajectory.

Before presenting the main results, we introduce two quantities that capture, respectively, the alignment between feature spaces and the accuracy of the proxy representations used in our analysis.

Definition 4.1 (Misalignment between DINOv2 and diffusion representations). For an image x and diffusion timestep t , we define the representation misalignment as

$$\text{MisREPA}(x, t) := \mathbb{E}_n \|f_{\text{DINOv2}}^{[n]}(x) - g_\phi(\text{DiffEnc}^{[n]}(x, t))\|_2^2,$$

where the expectation is taken uniformly over patch indices $n \in \{1, \dots, N\}$. Here $f_{\text{DINOv2}}^{[n]}(x)$ and $\text{DiffEnc}^{[n]}(x, t)$ denote the n -th patch features from the DINOv2 encoder and the diffusion model encoder, respectively. The mapping g_ϕ is the projection head introduced in Section 2.2¹.

Definition 4.2 (Proxy approximation error). For a ground-truth image x and its proxy approximation \bar{x} (defined in Section 3), we define the proxy approximation error as

$$\text{ApproxErr}(x, \bar{x}) := \mathbb{E}_n \|f_{\text{DINOv2}}^{[n]}(x) - f_{\text{DINOv2}}^{[n]}(\bar{x})\|_2^2,$$

where the expectation is taken uniformly over patch indices $n \in \{1, \dots, N\}$.

In practice, both quantities defined above are typically small. The feature misalignment $\text{MisREPA}(x, t)$ is mitigated through the explicit alignment of DINOv2 and diffusion encoder representations during training (Yu et al., 2024), while the approximation error $\text{ApproxErr}(x, \bar{x})$ is reduced by constructing proxy features \bar{x} that serves as reliable substitutes for the unavailable ground-truth features (see Section 3). Robustness of DINOv2 features to common

¹When the timestep argument is omitted, all t -dependent quantities are evaluated at $t = 0$. In particular, $\text{MisREPA}(x) \equiv \text{MisREPA}(x, 0)$ and $\text{DiffEnc}^{[n]}(x) \equiv \text{DiffEnc}^{[n]}(x, 0)$.

image degradations (Oquab et al., 2023), ensures that the resulting approximation gap remains small across the inverse problems we study.

Feature-Space Alignment: REPA as an MMD Surrogate.

Building on the definitions introduced above, we now establish a connection between the REPA regularizer and the statistical discrepancy between DINOv2 features of clean and reconstructed images. The proposition that follows formalizes this link by expressing the expected REPA score in terms of a feature-space divergence.

Proposition 4.3. Assume $x \sim p_X$ is a ground-truth image and $\hat{x} \sim p_{\hat{X}|Y}$ is its corresponding reconstruction, where $p_{\hat{X}|Y}$ is the distribution induced by any reconstruction method. Assume further that all DINOv2 feature embeddings are ℓ_2 -normalized. Let \bar{x} be a proxy approximation of x . Define the empirical mean DINOv2 feature embedding as

$$\mu_f(x) := \mathbb{E}_n [f_{\text{DINOv2}}^{[n]}(x)].$$

Then the expected REPA alignment satisfies

$$\begin{aligned} \mathbb{E}_{\hat{x}, \bar{x}}[\text{REPA}(\bar{x}, \hat{x})] &\leq 1 - \frac{1}{8} \text{MMD}_{\text{DINOv2}}(p_X, p_{\hat{X}}) \\ &+ \frac{1}{2} \mathbb{E}_{x, \bar{x}}[\text{ApproxErr}(x, \bar{x})] + \frac{1}{4} \mathbb{E}_{\hat{x}}[\text{MisREPA}(\hat{x})]. \end{aligned}$$

where

$$\text{MMD}_{\text{DINOv2}}(p_X, p_{\hat{X}}) = \|\mathbb{E}_x[\mu_f(x)] - \mathbb{E}_{\hat{x}}[\mu_f(\hat{x})]\|_2^2$$

is the maximum mean discrepancy between p_X and $p_{\hat{X}}$ in the DINOv2 feature space.

The proof is provided in the Appendix A.1. Proposition 4.3 establishes a connection between the representation alignment term and the maximum mean discrepancy (MMD) (Arbel et al., 2019), which quantifies perceptual divergence between feature distributions. This relationship indicates that maximizing the REPA term encourages the minimization of a divergence measure captured by the MMD together with additional penalties accounting for feature misalignment between diffusion and DINOv2 representations, as well as an approximation error arising from the use of proxy rather than ground-truth features for alignment.

When these terms are sufficiently small, Proposition 4.3 implies that maximizing the REPA term effectively corresponds to minimizing the maximum mean discrepancy (MMD) between the DINOv2 feature distributions of reconstructed and ground-truth images. This interpretation reveals that REPA regularization offers a principled, representation-based mechanism for enforcing perceptual consistency.

Effect of REPA on Internal Diffusion Representations.

We now study how a single REPA update influences the latent diffusion state relative to that of the clean image.

Proposition 4.4 (informal). *Consider an inverse problem with observation $y \in \mathbb{R}^m$ generated from a clean image $x \sim p_X$, and let \bar{x} denote the proxy image used by REPA. Let $z_t \in \mathbb{R}^d$ be the diffusion state at time t , $z_t^{(\text{REPA})}$ its REPA-regularized update. Let $z^* \in \mathbb{R}^d$ denote the latent variable associated with the clean image x . Under regularity assumptions on the Jacobian J_{DiffEnc} of the diffusion encoder DiffEnc and the mapping g_ϕ (see Appendix A.2), there exists a radius $r > 0$ such that, whenever $\|z_t - z^*\|_2 < r$, the REPA update induces a local contraction in the diffusion state space. In particular,*

$$\|z_t^{(\text{REPA})} - z^*\|_2 \leq C_1 \|z_t - z^*\|_2 + e(x),$$

$$e(x) := C_2 \left(\sqrt{\text{ApproxErr}(x, \bar{x})} + \sqrt{\text{MisREPA}(x)} \right),$$

where $C_1 \in (0, 1)$ and $C_2 > 0$ are constants depending on local conditioning properties of J_{DiffEnc} and g_ϕ .

The proof is provided in Appendix A.1. Proposition 4.4 characterizes how the REPA update modifies the latent diffusion state. The inequality shows that, when the current state z_t is reasonably close to the clean latent code z^* , a single REPA step contracts their distance up to two additive terms: the proxy approximation error $\text{ApproxErr}(x, \bar{x})$ and the representation misalignment $\text{MisREPA}(x)$, both of which are expected to be small in practice. This contraction therefore holds in a local regime around z^* , which corresponds in practice to stages of the diffusion process where the global structure of the reconstruction is already correct and the remaining errors are primarily fine-scale details and artifacts. In this regime, REPA acts as a perceptual regularizer, refining local image details and correcting artifacts that are not effectively addressed by the baseline update alone. Qualitative examples illustrating this behavior are provided in Figure 2 and the Appendix A.9.

Taken together, Propositions 4.3 and 4.4 indicate that REPA promotes perceptually meaningful reconstructions by steering the model toward regions of the latent space that reflect the semantic structure of natural images. Empirical evaluations in Section 5 reinforce this interpretation across multiple solvers and inverse problems.

5. Experimental Results

In this section, we present experimental results demonstrating the effectiveness of our alignment regularizer. We evaluate reconstruction quality using four widely adopted metrics: PSNR (peak signal-to-noise ratio), SSIM (structural similarity index) (Wang et al., 2004), LPIPS (learned perceptual image patch similarity) (Zhang et al., 2018), and FID (Fréchet Inception Distance) (Heusel et al., 2017). Experiments are conducted on both the ImageNet and FFHQ datasets (Deng et al., 2009; Karras et al., 2019), with FFHQ images resized

to 256×256 . All metrics for both datasets are averaged over 100 images from their corresponding validation splits.

We consider four inverse problems: super-resolution, box inpainting, Gaussian deblurring, and motion deblurring. Following the standard corruption operators used in state-of-the-art diffusion-based inverse problem methods (Chung et al., 2023; Zhang et al., 2025) we adopt the same degradation models in our experiments. For super-resolution, images are downsampled by a factor of 4. For box inpainting, we mask out a 128×128 square region. Gaussian deblurring is performed using a 61×61 kernel with standard deviation 3.0. Motion blur is simulated using a kernel with size 61×61 and intensity 0.5. For ImageNet we use additive Gaussian noise with standard deviation 0.01. For FFHQ we increase the noise level to 0.05 in order to obtain a more challenging reconstruction setting.

5.1. Effectiveness of the REPA Regularizer

This subsection evaluates how the REPA regularizer influences reconstruction quality by applying it to two representative latent-space solvers. To this end, we instantiate Algorithm 1 with Latent DPS and ReSample (Song et al., 2024), which differ in how the measurement-matching term is approximated. A detailed description of these methods and their integration with REPA is provided in Appendix A.2. For ImageNet experiments, we use the latent diffusion model trained with representation alignment from Yu et al. (2024), together with its pretrained MLP that projects internal diffusion representations into the DINOv2 feature space. For FFHQ, we train a representation-aligned SiT-BASE model from scratch following the same setup as Yu et al. (2024). In ImageNet experiments, the regularizer is applied to representations extracted after the eighth transformer block, while for FFHQ it is applied after the fourth block. For completeness, Appendix A.8 additionally reports results obtained when starting from an independently pretrained diffusion model. In this setting, we observe that incorporating the REPA regularizer continues to provide consistent perceptual benefits, although the gains are smaller compared to those achieved with alignment-pretrained models

Table 1 reports quantitative results across all four inverse problems. Incorporating REPA yields consistent improvements in perceptual metrics, notably reducing LPIPS and FID for both Latent DPS and ReSample while maintaining comparable PSNR and SSIM values. These results suggest that representation alignment guides the diffusion trajectory toward semantically consistent and perceptually realistic reconstructions that better match the target image. Figure 2 presents qualitative comparisons for box inpainting and Gaussian deblurring, where reconstructions obtained with REPA are visually sharper and more faithful to the ground truth, exhibiting fewer artifacts and clearer fine structures

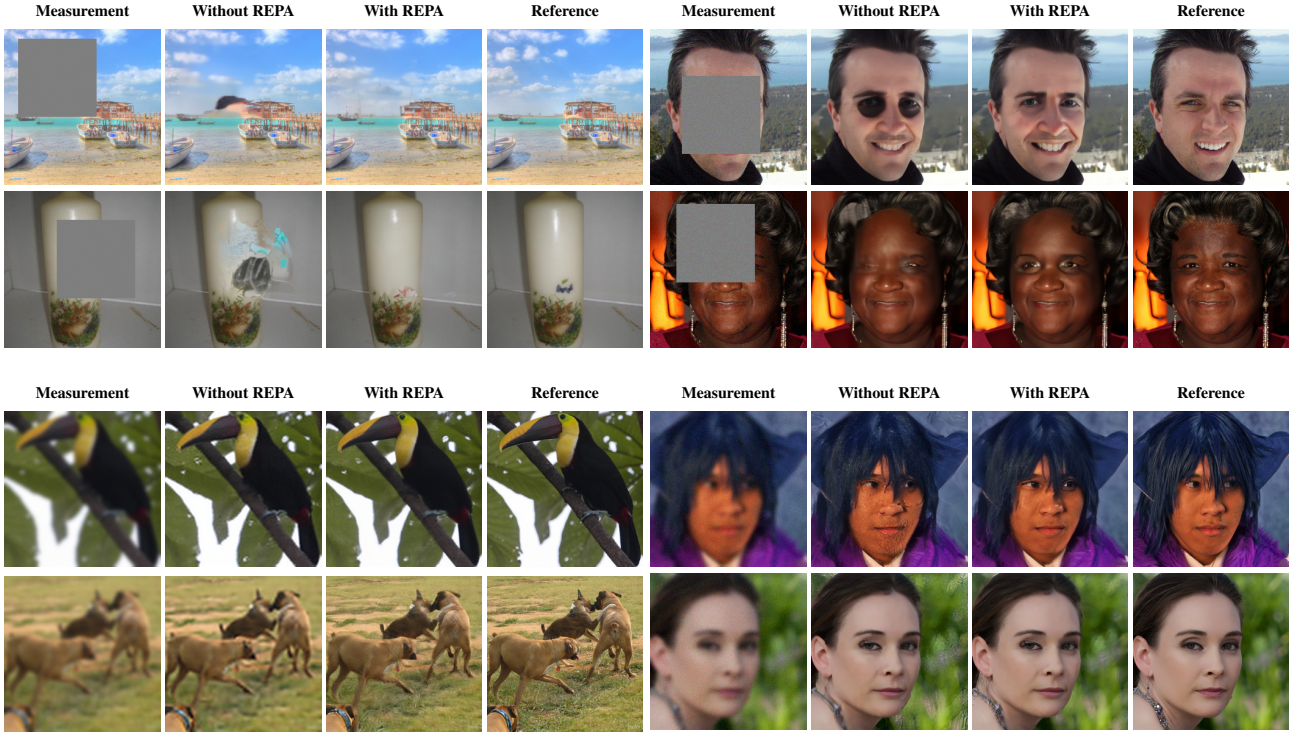


Figure 2. Qualitative comparison of inverse problem reconstruction with and without REPA. The top block corresponds to box inpainting and the bottom block to Gaussian deblurring; left panels show ImageNet results and right panels show FFHQ results. For each example, we show the measurement, the baseline reconstruction (Latent DPS or ReSample), the corresponding REPA-enhanced result, and the reference image. Within each panel, the first row corresponds to Latent DPS and the second row to ReSample.

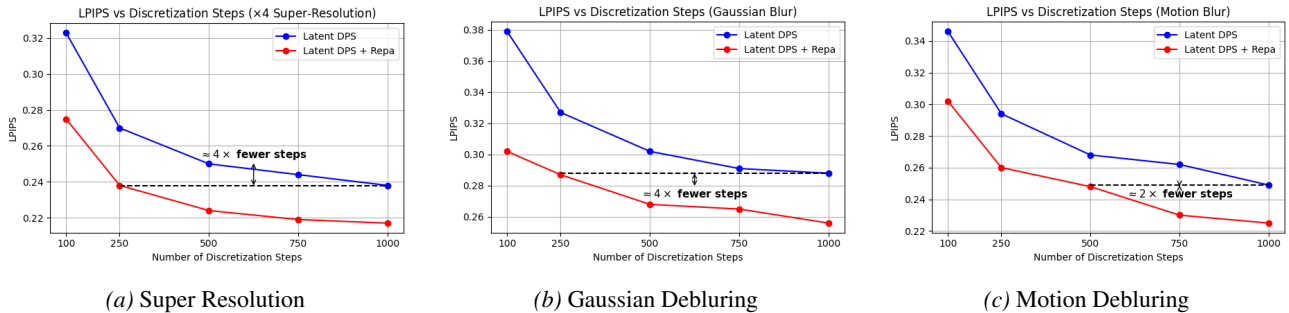


Figure 3. Comparison of LPIPS as a function of discretization steps for Latent DPS and Latent DPS + REPA. Using our regularizer, comparable performance is achieved with substantially fewer number of steps.

than those produced by the unregularized methods.

In addition to improving these latent solvers, we also compare our approach with other state-of-the-art reconstruction algorithms. For pixel-space methods, we consider DPS (Chung et al., 2023), evaluated using the pretrained diffusion model from Dhariwal & Nichol (2021). For latent diffusion baselines, we include Latent DAPS, implemented with the conditional ImageNet latent diffusion model from Rombach et al. (2022). As shown in Table 1, the proposed alignment regularizer consistently achieves state-of-the-art performance in perception-based metrics across

all inverse tasks and both datasets.

Effect of REPA with Varying Discretization Steps. Figure 3 illustrates how LPIPS varies with the number of discretization steps across three inverse problems. Incorporating the REPA regularizer consistently reduces perceptual error compared to Latent DPS alone. More importantly, REPA enables comparable or better perceptual quality with substantially fewer sampling steps: for example, in super-resolution and Gaussian deblurring, REPA achieves the same LPIPS with roughly $4\times$ fewer steps, while in motion deblurring it achieves the same level with about $2\times$ fewer steps. These re-

Table 1. Performance comparison on ImageNet and FFHQ across inverse tasks. ImageNet experiments use Gaussian noise with $\sigma = 0.01$, while FFHQ uses $\sigma = 0.05$. Lower is better for LPIPS/FID, higher is better for PSNR/SSIM. Best per dataset and task in **bold**.

| Task | Method | ImageNet | | | | FFHQ | | | |
|-----------------|-------------------|--------------|--------------|--------------|--------------|--------------|--------------|--------------|--------------|
| | | LPIPS↓ | FID↓ | PSNR↑ | SSIM↑ | LPIPS↓ | FID↓ | PSNR↑ | SSIM↑ |
| 4× SR | Latent DPS | 0.238 | 123.82 | 26.88 | 0.732 | 0.188 | 56.69 | 28.99 | 0.814 |
| | Latent DPS + REPA | 0.217 | 86.88 | 26.82 | 0.731 | 0.177 | 51.27 | 29.12 | 0.819 |
| | Resample | 0.208 | 97.02 | 26.70 | 0.736 | 0.178 | 52.82 | 29.06 | 0.814 |
| | Resample + REPA | 0.197 | 74.70 | 26.99 | 0.740 | 0.167 | 46.36 | 29.17 | 0.818 |
| | DPS | 0.244 | 92.13 | 24.42 | 0.681 | 0.182 | 54.19 | 27.67 | 0.804 |
| | Latent DAPS | 0.252 | 120.57 | 27.13 | 0.744 | 0.206 | 74.82 | 28.95 | 0.820 |
| Inpainting | Latent DPS | 0.151 | 116.53 | 20.53 | 0.822 | 0.192 | 65.89 | 23.55 | 0.785 |
| | Latent DPS + REPA | 0.139 | 88.69 | 20.45 | 0.824 | 0.178 | 57.04 | 23.83 | 0.784 |
| | Resample | 0.153 | 121.98 | 20.53 | 0.812 | 0.192 | 67.99 | 23.86 | 0.792 |
| | Resample + REPA | 0.143 | 87.15 | 20.79 | 0.827 | 0.178 | 61.97 | 24.01 | 0.793 |
| | DPS | 0.191 | 97.95 | 19.11 | 0.769 | 0.190 | 104.53 | 20.02 | 0.786 |
| | Latent DAPS | 0.318 | 188.44 | 21.21 | 0.718 | 0.210 | 89.21 | 24.39 | 0.817 |
| Gaussian Deblur | Latent DPS | 0.288 | 152.96 | 25.76 | 0.648 | 0.192 | 60.65 | 28.15 | 0.783 |
| | Latent DPS + REPA | 0.256 | 102.99 | 25.66 | 0.669 | 0.186 | 55.53 | 28.21 | 0.787 |
| | Resample | 0.259 | 115.47 | 26.19 | 0.699 | 0.172 | 56.41 | 27.01 | 0.753 |
| | Resample + REPA | 0.223 | 89.67 | 26.49 | 0.707 | 0.168 | 52.73 | 27.17 | 0.756 |
| | DPS | 0.366 | 157.73 | 19.55 | 0.461 | 0.177 | 53.18 | 27.19 | 0.789 |
| | Latent DAPS | 0.291 | 159.67 | 26.02 | 0.692 | 0.229 | 104.43 | 28.73 | 0.809 |
| Motion Deblur | Latent DPS | 0.249 | 129.08 | 27.19 | 0.738 | 0.170 | 52.14 | 27.20 | 0.773 |
| | Latent DPS + REPA | 0.225 | 90.23 | 27.01 | 0.735 | 0.165 | 47.18 | 27.16 | 0.772 |
| | Resample | 0.210 | 89.95 | 27.57 | 0.739 | 0.157 | 52.19 | 28.36 | 0.791 |
| | Resample + REPA | 0.192 | 75.11 | 27.80 | 0.766 | 0.151 | 50.02 | 28.41 | 0.794 |
| | DPS | 0.242 | 89.06 | 24.17 | 0.678 | 0.146 | 43.32 | 27.28 | 0.793 |
| | Latent DAPS | 0.264 | 125.18 | 27.25 | 0.744 | 0.191 | 76.21 | 29.77 | 0.836 |

sults highlight the efficiency gains provided by our method, reducing computational cost without sacrificing the reconstruction quality of the baseline method.

REPA vs Guidance in the DINO feature space. To further showcase the benefits of representation alignment, Appendix A.7 compares REPA to a variant that enforces consistency directly in the DINOv2 feature space of the reconstructed image, without aligning the diffusion model’s internal states. Concretely, the feature-only variant applies the following guidance at each timestep:

$$z_{t-1} \leftarrow z_{t-1} + \lambda \nabla_{z_t} \sum_{n=1}^N \cos\left(c_{\text{proxy}}^{[n]}, f_{\text{DINOv2}}^{[n]}(\hat{x}_0(z_t))\right),$$

where $\hat{x}_0(z_t) := \mathcal{D}(\mathbb{E}[z_0 | z_t])$ denotes the decoded prediction of the clean image at timestep t . This approach relies solely on the DINOv2 features of the decoded image. In contrast, REPA injects representation alignment directly into the diffusion dynamics by aligning the model’s internal representations with DINOv2 features throughout the reverse process. As observed in Appendix A.7, this feature-only guidance performs worse in practice. A natural explanation through the lens of Proposition 4.4 is that the composite mapping $z_t \mapsto \mathbb{E}[z_0 | z_t] \mapsto \mathcal{D}(\mathbb{E}[z_0 | z_t]) \mapsto f_{\text{DINOv2}}(\cdot)$ is significantly more ill-conditioned than the lightweight patchwise projection used in REPA, resulting in weaker and

less stable gradients with respect to the diffusion state.

6. Conclusions

In this work, we introduced *representation alignment* as a principled framework for solving inverse problems with diffusion- and flow-based generative models. By aligning internal model representations with features from a pre-trained DINOv2 encoder, our method provides a strong semantic prior that guides the reconstruction process toward perceptually meaningful solutions. We further offered theoretical insights into this mechanism, showing that REPA regularization corresponds to minimizing a divergence in the DINOv2 feature space and reduces the discrepancy between the current and the clean latent state. These results elucidate why re alignment can enhance perceptual fidelity in inverse problem settings. Overall, our study demonstrates that representation alignment constitutes a flexible and effective tool for improving generative inverse problem solvers, yielding benefits at inference time and integrate seamlessly with a range of diffusion- and flow-based methods.

Impact Statement

This paper presents work aimed at advancing the field of machine learning, with a focus on improving the reliability of inverse problem solvers through representation alignment

in pretrained diffusion and flow based models. While this work may have broader societal implications, we do not identify any that require specific discussion here.

References

- Albergo, M. S., Boffi, N. M., and Vanden-Eijnden, E. Stochastic interpolants: A unifying framework for flows and diffusions. *arXiv preprint arXiv:2303.08797*, 2023.
- Arbel, M., Korba, A., Salim, A., and Gretton, A. Maximum mean discrepancy gradient flow. *Advances in Neural Information Processing Systems*, 32, 2019.
- Assran, M., Duval, Q., Misra, I., Bojanowski, P., Vincent, P., Rabat, M., LeCun, Y., and Ballas, N. Self-supervised learning from images with a joint-embedding predictive architecture. In *Proceedings of the IEEE/CVF Conference on Computer Vision and Pattern Recognition*, pp. 15619–15629, 2023.
- Blattmann, A., Rombach, R., Oktay, K., Müller, J., and Ommer, B. Retrieval-augmented diffusion models. *Advances in Neural Information Processing Systems*, 35: 15309–15324, 2022.
- Chung, H., Kim, J., McCann, M. T., Klasky, M. L., and Ye, J. C. Diffusion posterior sampling for general noisy inverse problems. In *The Eleventh International Conference on Learning Representations*, 2023.
- Daras, G., Chung, H., Lai, C.-H., Mitsufuji, Y., Ye, J. C., Milanfar, P., Dimakis, A. G., and Delbraccio, M. A survey on diffusion models for inverse problems. *arXiv preprint arXiv:2410.00083*, 2024.
- Deng, J., Dong, W., Socher, R., Li, L.-J., Li, K., and Fei-Fei, L. Imagenet: A large-scale hierarchical image database. In *2009 IEEE conference on computer vision and pattern recognition*, pp. 248–255. Ieee, 2009.
- Dhariwal, P. and Nichol, A. Diffusion models beat gans on image synthesis. *Advances in neural information processing systems*, 34:8780–8794, 2021.
- Dosovitskiy, A. and Brox, T. Generating images with perceptual similarity metrics based on deep networks. *Advances in Neural Information Processing Systems*, 29, 2016.
- Esser, P., Kulal, S., Blattmann, A., Entezari, R., Müller, J., Saini, H., Levi, Y., Lorenz, D., Sauer, A., Boesel, F., et al. Scaling rectified flow transformers for high-resolution image synthesis. In *Proceedings of the 41st International Conference on Machine Learning*, pp. 12606–12633, 2024.
- Fu, S., Tamir, N., Sundaram, S., Chai, L., Zhang, R., Dekel, T., and Isola, P. Dreamsim: Learning new dimensions of human visual similarity using synthetic data. *arXiv preprint arXiv:2306.09344*, 2023.
- Heusel, M., Ramsauer, H., Unterthiner, T., Nessler, B., and Hochreiter, S. Gans trained by a two time-scale update rule converge to a local nash equilibrium. *Advances in neural information processing systems*, 30, 2017.
- Ho, J., Jain, A., and Abbeel, P. Denoising diffusion probabilistic models. *Advances in neural information processing systems*, 33:6840–6851, 2020.
- Hu, V. T., Zhang, D. W., Asano, Y. M., Burghouts, G. J., and Snoek, C. G. Self-guided diffusion models. In *Proceedings of the IEEE/CVF Conference on Computer Vision and Pattern Recognition*, pp. 18413–18422, 2023.
- Hyvärinen, A. and Dayan, P. Estimation of non-normalized statistical models by score matching. *Journal of Machine Learning Research*, 6(4), 2005.
- Karras, T., Laine, S., and Aila, T. A style-based generator architecture for generative adversarial networks. In *Proceedings of the IEEE/CVF conference on computer vision and pattern recognition*, pp. 4401–4410, 2019.
- Lai, C.-H., Song, Y., Kim, D., Mitsufuji, Y., and Ermon, S. The principles of diffusion models. *arXiv preprint arXiv:2510.21890*, 2025.
- Leng, X., Singh, J., Hou, Y., Xing, Z., Xie, S., and Zheng, L. Repa-e: Unlocking vae for end-to-end tuning with latent diffusion transformers. *arXiv preprint arXiv:2504.10483*, 2025.
- Li, A. C., Prabhudesai, M., Duggal, S., Brown, E., and Pathak, D. Your diffusion model is secretly a zero-shot classifier. In *Proceedings of the IEEE/CVF International Conference on Computer Vision*, pp. 2206–2217, 2023.
- Li, T., Katabi, D., and He, K. Return of unconditional generation: A self-supervised representation generation method. *Advances in Neural Information Processing Systems*, 37:125441–125468, 2024.
- Lipman, Y., Chen, R. T., Ben-Hamu, H., Nickel, M., and Le, M. Flow matching for generative modeling. In *11th International Conference on Learning Representations, ICLR 2023*, 2023.
- Liu, X., Gong, C., and Liu, Q. Flow straight and fast: Learning to generate and transfer data with rectified flow. In *The Eleventh International Conference on Learning Representations (ICLR)*, 2023.
- Oquab, M., Darcet, T., Moutakanni, T., Vo, H., Szafraniec, M., Khalidov, V., Fernandez, P., Haziza, D., Massa, F., El-Nouby, A., et al. Dinov2: Learning robust visual features

- without supervision. *arXiv preprint arXiv:2304.07193*, 2023.
- Pachebat, J., Conforti, G., Durmus, A., and Janati, Y. Iterative tilting for diffusion fine-tuning. *arXiv preprint arXiv:2512.03234*, 2025.
- Patel, M., Wen, S., Metaxas, D. N., and Yang, Y. Steering rectified flow models in the vector field for controlled image generation. *arXiv preprint arXiv:2412.00100*, 2024.
- Raphaelli, R., Man, S., and Elad, M. Silo: Solving inverse problems with latent operators. In *Proceedings of the IEEE/CVF International Conference on Computer Vision*, pp. 10570–10580, 2025.
- Rombach, R., Blattmann, A., Lorenz, D., Esser, P., and Ommer, B. High-resolution image synthesis with latent diffusion models. In *Proceedings of the IEEE/CVF conference on computer vision and pattern recognition*, pp. 10684–10695, 2022.
- Rout, L., Raoof, N., Daras, G., Caramanis, C., Dimakis, A., and Shakkottai, S. Solving linear inverse problems provably via posterior sampling with latent diffusion models. In *Thirty-seventh Conference on Neural Information Processing Systems*, 2023.
- Sheynin, S., Ashual, O., Polyak, A., Singer, U., Gafni, O., Nachmani, E., and Taigman, Y. Knn-diffusion: Image generation via large-scale retrieval. *arXiv preprint arXiv:2204.02849*, 2022.
- Siméoni, O., Vo, H. V., Seitzer, M., Baldassarre, F., Oquab, M., Jose, C., Khalidov, V., Szafraniec, M., Yi, S., Ramamonjisoa, M., et al. Dinov3. *arXiv preprint arXiv:2508.10104*, 2025.
- Sohl-Dickstein, J., Weiss, E., Maheswaranathan, N., and Ganguli, S. Deep unsupervised learning using nonequilibrium thermodynamics. In *International conference on machine learning*, pp. 2256–2265. PMLR, 2015.
- Song, B., Kwon, S. M., Zhang, Z., Hu, X., Qu, Q., and Shen, L. Solving inverse problems with latent diffusion models via hard data consistency. In *The Twelfth International Conference on Learning Representations*, 2024.
- Song, J., Meng, C., and Ermon, S. Denoising diffusion implicit models. In *International Conference on Learning Representations*, 2021.
- Thaker, D., Goyal, A., and Vidal, R. Frequency-guided posterior sampling for diffusion-based image restoration. In *Proceedings of the IEEE/CVF International Conference on Computer Vision*, pp. 12873–12882, 2025.
- Tian, Y., Chen, H., Zheng, M., Liang, Y., Xu, C., and Wang, Y. U-repa: Aligning diffusion u-nets to vits. *arXiv preprint arXiv:2503.18414*, 2025.
- Wang, C., Zhou, C., Gupta, S., Lin, Z., Jegelka, S., Bates, S., and Jaakkola, T. Learning diffusion models with flexible representation guidance. *arXiv preprint arXiv:2507.08980*, 2025a.
- Wang, Z., Bovik, A. C., Sheikh, H. R., and Simoncelli, E. P. Image quality assessment: from error visibility to structural similarity. *IEEE transactions on image processing*, 13(4):600–612, 2004.
- Wang, Z., Zhao, W., Zhou, Y., Li, Z., Liang, Z., Shi, M., Zhao, X., Zhou, P., Zhang, K., Wang, Z., et al. Repa works until it doesn't: Early-stopped, holistic alignment supercharges diffusion training. *arXiv preprint arXiv:2505.16792*, 2025b.
- Xiang, W., Yang, H., Huang, D., and Wang, Y. Denoising diffusion autoencoders are unified self-supervised learners. In *Proceedings of the IEEE/CVF International Conference on Computer Vision*, 2023.
- Xu, W., Yue, X., Wang, Z., Teng, Y., Zhang, W., Liu, X., Zhou, L., Ouyang, W., and Bai, L. Exploring representation-aligned latent space for better generation. *arXiv preprint arXiv:2502.00359*, 2025.
- Yao, J., Yang, B., and Wang, X. Reconstruction vs. generation: Taming optimization dilemma in latent diffusion models. In *Proceedings of the Computer Vision and Pattern Recognition Conference*, pp. 15703–15712, 2025.
- Yu, S., Kwak, S., Jang, H., Jeong, J., Huang, J., Shin, J., and Xie, S. Representation alignment for generation: Training diffusion transformers is easier than you think. *arXiv preprint arXiv:2410.06940*, 2024.
- Zhang, B., Chu, W., Berner, J., Meng, C., Anandkumar, A., and Song, Y. Improving diffusion inverse problem solving with decoupled noise annealing. In *Proceedings of the Computer Vision and Pattern Recognition Conference*, pp. 20895–20905, 2025.
- Zhang, R., Isola, P., Efros, A. A., Shechtman, E., and Wang, O. The unreasonable effectiveness of deep features as a perceptual metric. In *Proceedings of the IEEE conference on computer vision and pattern recognition*, pp. 586–595, 2018.

A. Appendix.

A.1. Proofs

Proposition A.1. Assume $x \sim p_X$ is a ground-truth image and $\hat{x} \sim p_{\hat{X}|Y}$ is its corresponding reconstruction, where $p_{\hat{X}|Y}$ is the distribution induced by any reconstruction method. Assume further that all DINOv2 feature embeddings are ℓ_2 -normalized. Let \bar{x} be a proxy approximation of x . Define the empirical mean DINOv2 feature embedding as

$$\mu_f(x) := \mathbb{E}_n \left[f_{\text{DINOv2}}^{[n]}(x) \right].$$

Then the expected REPA alignment satisfies

$$\begin{aligned} \mathbb{E}_{\hat{x}, \bar{x}}[\text{REPA}(\bar{x}, \hat{x})] &\leq 1 - \frac{1}{8} \text{MMD}_{\text{DINOv2}}(p_X, p_{\hat{X}}) \\ &+ \frac{1}{2} \mathbb{E}_{x, \bar{x}}[\text{ApproxErr}(x, \bar{x})] + \frac{1}{4} \mathbb{E}_{\hat{x}}[\text{MisREPA}(\hat{x})]. \end{aligned}$$

where

$$\text{MMD}_{\text{DINOv2}}(p_X, p_{\hat{X}}) = \left\| \mathbb{E}_x[\mu_f(x)] - \mathbb{E}_{\hat{x}}[\mu_f(\hat{x})] \right\|_2^2$$

is the maximum mean discrepancy between p_X and $p_{\hat{X}}$ in the DINOv2 feature space.

Proof.

$$\text{REPA}(\bar{x}, \hat{x}) = \frac{1}{N} \sum_{n=1}^N \cos \left(f_{\text{DINOv2}}^{[n]}(\bar{x}), g_\phi(\text{DIFFENC}^{[n]}(\hat{x})) \right),$$

Assume the features are ℓ_2 -normalized. Then for each n ,

$$\cos \left(f_{\text{DINOv2}}^{[n]}(\bar{x}), g_\phi(\text{DIFFENC}^{[n]}(\hat{x})) \right) = 1 - \frac{1}{2} \left\| f_{\text{DINOv2}}^{[n]}(\bar{x}) - g_\phi(\text{DIFFENC}^{[n]}(\hat{x})) \right\|_2^2,$$

and hence

$$\text{REPA}(\bar{x}, \hat{x}) = 1 - \frac{1}{2N} \sum_{n=1}^N \left\| f_{\text{DINOv2}}^{[n]}(\bar{x}) - g_\phi(\text{DIFFENC}^{[n]}(\hat{x})) \right\|_2^2.$$

Let the empirical (mean) feature embeddings be

$$\begin{aligned} \mu_f(x) &:= \frac{1}{N} \sum_{n=1}^N f_{\text{DINOv2}}^{[n]}(x), & \mu_f(\bar{x}) &:= \frac{1}{N} \sum_{n=1}^N f_{\text{DINOv2}}^{[n]}(\bar{x}), \\ \mu_f(\hat{x}) &:= \frac{1}{N} \sum_{n=1}^N f_{\text{DINOv2}}^{[n]}(\hat{x}), & \mu_g(\hat{x}) &:= \frac{1}{N} \sum_{n=1}^N g_\phi(\text{DIFFENC}^{[n]}(\hat{x})). \end{aligned}$$

From Jensen's inequality for the squared norm :

$$\left\| \mu_f(x) - \mu_f(\hat{x}) \right\|_2^2 \leq 2 \left\| \mu_f(x) - \mu_g(\hat{x}) \right\|_2^2 + 2 \left\| \mu_f(\hat{x}) - \mu_g(\hat{x}) \right\|_2^2.$$

Moreover,

$$\left\| \mu_f(x) - \mu_g(\hat{x}) \right\|_2^2 = \left\| \frac{1}{N} \sum_{n=1}^N (f_{\text{DINOv2}}^{[n]}(x) - g_\phi(\text{DIFFENC}^{[n]}(\hat{x}))) \right\|_2^2 \leq \frac{1}{N} \sum_{n=1}^N \left\| f_{\text{DINOv2}}^{[n]}(x) - g_\phi(\text{DIFFENC}^{[n]}(\hat{x})) \right\|_2^2,$$

and similarly

$$\left\| \mu_f(\hat{x}) - \mu_g(\hat{x}) \right\|_2^2 \leq \frac{1}{N} \sum_{n=1}^N \left\| f_{\text{DINOv2}}^{[n]}(\hat{x}) - g_\phi(\text{DIFFENC}^{[n]}(\hat{x})) \right\|_2^2 = \text{MisREPA}(\hat{x}).$$

Combining the two yields

$$\begin{aligned} \|\mu_f(x) - \mu_f(\hat{x})\|_2^2 &\leq \frac{2}{N} \sum_{n=1}^N \|f_{\text{DINOv2}}^{[n]}(x) - g_\phi(\text{DIFFENC}^{[n]}(\hat{x}))\|_2^2 + 2 \text{MisREPA}(\hat{x}) \\ &\leq \frac{4}{N} \sum_{n=1}^N \|f_{\text{DINOv2}}^{[n]}(\bar{x}) - g_\phi(\text{DIFFENC}^{[n]}(\hat{x}))\|_2^2 + \frac{4}{N} \sum_{n=1}^N \|f_{\text{DINOv2}}^{[n]}(x) - f_{\text{DINOv2}}^{[n]}(\bar{x})\|_2^2 + 2 \text{MisREPA}(\hat{x}). \end{aligned} \quad (9)$$

$$= \frac{4}{N} \sum_{n=1}^N \|f_{\text{DINOv2}}^{[n]}(\bar{x}) - g_\phi(\text{DIFFENC}^{[n]}(\hat{x}))\|_2^2 + 4 \text{ApproxErr}(x, \bar{x}) + 2 \text{MisREPA}(\hat{x}). \quad (10)$$

Using the cosine-squared identity for unit-norm features,

$$\sum_{n=1}^N \|f_{\text{DINOv2}}^{[n]}(\bar{x}) - g_\phi(\text{DIFFENC}^{[n]}(\hat{x}))\|_2^2 = 2N(1 - \text{REPA}(\bar{x}, \hat{x})),$$

$$\|\mu_f(x) - \mu_f(\hat{x})\|_2^2 \leq 8(1 - \text{REPA}(\bar{x}, \hat{x})) + 4 \text{ApproxErr}(x, \bar{x}) + 2 \text{MisREPA}(\hat{x}).$$

Rearranging gives the bound

$$\text{REPA}(\bar{x}, \hat{x}) \leq 1 - \frac{1}{8} \|\mu_f(x) - \mu_f(\hat{x})\|_2^2 + \frac{1}{2} \text{ApproxErr}(x, \bar{x}) + \frac{1}{4} \text{MisREPA}(\hat{x}).$$

Taking expectations over $x \sim p_X$, and $\hat{x} \sim p_{\hat{X}}$, and using the convexity of the squared norm,

$$\mathbb{E}[\|\mu_f(x) - \mu_f(\hat{x})\|_2^2] \geq \|\mathbb{E}_x[\mu_f(x)] - \mathbb{E}_{\hat{x}}[\mu_f(\hat{x})]\|_2^2 = \text{MMD}_{\text{DINOv2}}(p_X, p_{\hat{X}}),$$

we obtain

$$\mathbb{E}_{\hat{x}, \bar{x}}[\text{REPA}(\bar{x}, \hat{x})] \leq 1 - \frac{1}{8} \text{MMD}_{\text{DINOv2}}(p_X, p_{\hat{X}}) + \frac{1}{2} \mathbb{E}_{x, \bar{x}}[\text{ApproxErr}(x, \bar{x})] + \frac{1}{4} \mathbb{E}_{\hat{x}}[\text{MisREPA}(\hat{x})], \quad (11)$$

Assumption A.2 (Regularity of the diffusion encoder and REPA projection). We operate under the following regularity and conditioning assumptions on the diffusion feature extractor and the REPA projection. For notational simplicity in the analysis, we introduce an operator corresponding to the vectorized diffusion encoder. Let $\tilde{G}(\cdot) := \text{vec}(\text{DIFFENC}(\cdot, t)) : \mathbb{R}^d \rightarrow \mathbb{R}^{ND}$ denote the vectorized diffusion feature extractor at timestep t , and let $\tilde{g}_\phi : \mathbb{R}^{ND} \rightarrow \mathbb{R}^{ND}$ denote the patchwise lift of the projection head $g_\phi : \mathbb{R}^D \rightarrow \mathbb{R}^D$. Fix two diffusion states $z_t, z^* \in \mathbb{R}^d$ and define $u_t := \tilde{G}(z_t)$ and $u^* := \tilde{G}(z^*)$. Let

$$B := \{z^* + s(z_t - z^*) : s \in [0, 1]\} \quad \text{and} \quad \mathcal{U} := \{\tilde{G}(z) : z \in B\}.$$

A.2.1 The mapping \tilde{G} is differentiable, and its Jacobian $J_{\tilde{G}}(z) \in \mathbb{R}^{(ND) \times d}$ is Lipschitz continuous on B with Lipschitz constant L_G .

A.2.2 There exist constants $m_G > 0$ and $M_G < \infty$ such that

$$J_{\tilde{G}}(z_t)^\top J_{\tilde{G}}(z_t) \succeq m_G^2 I_d, \quad \|J_{\tilde{G}}(z)\|_2 \leq M_G \quad \text{for all } z \in B.$$

A.2.3 The mapping \tilde{g}_ϕ is differentiable, and its Jacobian $J_{\tilde{g}_\phi}(u) \in \mathbb{R}^{(ND) \times (ND)}$ is uniformly well-conditioned at u_t : there exists a constant $m_\phi > 0$ such that

$$J_{\tilde{g}_\phi}(u_t)^\top J_{\tilde{g}_\phi}(u_t) \succeq m_\phi^2 I_{ND}, \quad \|J_{\tilde{g}_\phi}(u)\|_2 \leq M_\phi \quad \text{for all } u \in \mathcal{U}.$$

A.2.4 The Jacobian $J_{\tilde{g}_\phi}$ is Lipschitz continuous on \mathcal{U} with Lipschitz constant L_ϕ .

Proposition A.3 (Local contraction of REPA in the diffusion state space). *Consider an inverse problem in which an observation $y \in \mathbb{R}^m$ is generated from a ground-truth image $x \sim p_X$, and let $\bar{x} \sim p_{\bar{X}}$ denote the proxy approximation used during REPA. Let $z_t \in \mathbb{R}^d$ be the diffusion state at timestep t produced by Algorithm 1, and let $z_t^{(\text{REPA})}$ denote the diffusion state after applying the REPA regularization update. Let $z^* \in \mathbb{R}^d$ denote the latent variable associated with the clean image x . Under Assumptions A_1 – A_4 , define*

$$r := \frac{2m_G^2 m_\phi^2}{L_\phi M_G^3 M_\phi + L_G M_\phi^2 M_G}.$$

If $\|z_t - z^*\|_2 < r$, then there exists a stepsize

$$0 < \lambda \leq \frac{1}{2M_G^2 M_\phi^2}$$

such that the REPA update induces a local contraction in the diffusion state space. In particular,

$$\|z_t^{(\text{REPA})} - z^*\|_2 \leq C_1 \|z_t - z^*\|_2 + C_2 \left(\sqrt{\text{ApproxErr}(x, \bar{x})} + \sqrt{\text{MisREPA}(x)} \right),$$

where

$$C_1 := 1 - \lambda m_G m_\phi \in (0, 1), \quad C_2 := 2 \lambda M_G M_\phi \sqrt{N}.$$

Proof. We first rewrite all quantities in vectorized form. Let $\text{vec}(\cdot)$ denote the operator that stacks the rows of a matrix into a single vector. For any matrix $H \in \mathbb{R}^{k_1 \times k_2}$, define

$$\tilde{H} := \text{vec}(H) \in \mathbb{R}^{k_1 k_2}.$$

For the DINOv2 features $f_{\text{DINOv2}}(x) \in \mathbb{R}^{N \times D}$ we write

$$\tilde{f}(x) := \text{vec}(f_{\text{DINOv2}}(x)) \in \mathbb{R}^{ND}.$$

For the diffusion-model feature extractor $\text{DIFFENC} : \mathbb{R}^d \times \mathbb{R} \rightarrow \mathbb{R}^{N \times D}$, we define its vectorized form by

$$\tilde{G}(z_t) := \text{vec}(\text{DIFFENC}(z_t, t)) \in \mathbb{R}^{ND}.$$

Recall that $\phi : \mathbb{R}^D \rightarrow \mathbb{R}^D$ is differentiable. Its lifted Jacobian acts patchwise and satisfies

$$J_{\tilde{g}_\phi}(\tilde{G}(z_t)) = I_N \otimes J_\phi(G_2(z_t)).$$

The REPA update is given by

$$z_t^{(\text{REPA})} = z_t - \lambda \nabla_{z_t} \|\tilde{f}(\bar{x}) - \tilde{g}_\phi(\tilde{G}(z_t))\|_2^2.$$

By the chain rule,

$$z_t^{(\text{REPA})} = z_t + 2\lambda J_{\tilde{G}}(z_t)^\top J_{\tilde{g}_\phi}(\tilde{G}(z_t))^\top (\tilde{f}(\bar{x}) - \tilde{g}_\phi(\tilde{G}(z_t))).$$

Subtracting z^* from both sides yields

$$z_t^{(\text{REPA})} - z^* = z_t - z^* + 2\lambda J_{\tilde{G}}(z_t)^\top J_{\tilde{g}_\phi}(\tilde{G}(z_t))^\top (\tilde{f}(\bar{x}) - \tilde{g}_\phi(\tilde{G}(z_t))).$$

We now add and subtract $\tilde{f}(x)$ and $\tilde{g}_\phi(\tilde{G}(z^*))$ inside the parentheses:

$$\begin{aligned} z_t^{(\text{REPA})} - z^* &= (z_t - z^*) - 2\lambda J_{\tilde{G}}(z_t)^\top J_{\tilde{g}_\phi}(\tilde{G}(z_t))^\top (\tilde{g}_\phi(\tilde{G}(z_t)) - \tilde{g}_\phi(\tilde{G}(z^*))) \\ &\quad + 2\lambda J_{\tilde{G}}(z_t)^\top J_{\tilde{g}_\phi}(\tilde{G}(z_t))^\top (\tilde{f}(\bar{x}) - \tilde{f}(x)) \\ &\quad + 2\lambda J_{\tilde{G}}(z_t)^\top J_{\tilde{g}_\phi}(\tilde{G}(z_t))^\top (\tilde{f}(x) - \tilde{g}_\phi(\tilde{G}(z^*))). \end{aligned} \tag{12}$$

We define the *contractive part* as

$$\mathcal{T}_t := (z_t - z^*) - 2\lambda J_{\tilde{G}}(z_t)^\top J_{\tilde{g}_\phi}(\tilde{G}(z_t))^\top (\tilde{g}_\phi(\tilde{G}(z_t)) - \tilde{g}_\phi(\tilde{G}(z^*))).$$

Applying the fundamental theorem of calculus to $u \mapsto \tilde{g}_\phi(u)$ along $u(s) = \tilde{G}(z(s))$ with $z(s) = z^* + s(z_t - z^*)$, $s \in [0, 1]$, yields

$$\tilde{g}_\phi(\tilde{G}(z_t)) - \tilde{g}_\phi(\tilde{G}(z^*)) = \int_0^1 J_{\tilde{g}_\phi}(\tilde{G}(z(s))) J_{\tilde{G}}(z(s)) (z_t - z^*) ds.$$

Substituting into the definition of \mathcal{T}_t gives

$$\mathcal{T}_t = \left[I - 2\lambda \int_0^1 J_{\tilde{G}}(z_t)^\top J_{\tilde{g}_\phi}(\tilde{G}(z_t))^\top J_{\tilde{g}_\phi}(\tilde{G}(z(s))) J_{\tilde{G}}(z(s)) ds \right] (z_t - z^*). \quad (13)$$

Add and subtract $J_{\tilde{g}_\phi}(\tilde{G}(z_t)) J_{\tilde{G}}(z_t)$ inside the integral to obtain

$$\begin{aligned} \mathcal{T}_t &= \left[I - 2\lambda J_{\tilde{G}}(z_t)^\top J_{\tilde{g}_\phi}(\tilde{G}(z_t))^\top J_{\tilde{g}_\phi}(\tilde{G}(z_t)) J_{\tilde{G}}(z_t) \right] (z_t - z^*) \\ &\quad - 2\lambda \left[\int_0^1 J_{\tilde{G}}(z_t)^\top J_{\tilde{g}_\phi}(\tilde{G}(z_t))^\top \left(J_{\tilde{g}_\phi}(\tilde{G}(z(s))) J_{\tilde{G}}(z(s)) - J_{\tilde{g}_\phi}(\tilde{G}(z_t)) J_{\tilde{G}}(z_t) \right) ds \right] (z_t - z^*). \end{aligned} \quad (14)$$

Taking Euclidean norms in (14) and using the triangle inequality gives

$$\begin{aligned} \|\mathcal{T}_t\|_2 &\leq \left\| I - 2\lambda J_{\tilde{G}}(z_t)^\top J_{\tilde{g}_\phi}(\tilde{G}(z_t))^\top J_{\tilde{g}_\phi}(\tilde{G}(z_t)) J_{\tilde{G}}(z_t) \right\|_2 \|z_t - z^*\|_2 \\ &\quad + 2\lambda \left\| \int_0^1 J_{\tilde{G}}(z_t)^\top J_{\tilde{g}_\phi}(\tilde{G}(z_t))^\top \left(J_{\tilde{g}_\phi}(\tilde{G}(z(s))) J_{\tilde{G}}(z(s)) - J_{\tilde{g}_\phi}(\tilde{G}(z_t)) J_{\tilde{G}}(z_t) \right) ds \right\|_2 \|z_t - z^*\|_2. \end{aligned} \quad (15)$$

Moreover, by submultiplicativity of the spectral norm and $\left\| \int_0^1 A(s) ds \right\|_2 \leq \int_0^1 \|A(s)\|_2 ds$, the second term can be bounded as

$$\left\| \int_0^1 J_{\tilde{G}}(z_t)^\top J_{\tilde{g}_\phi}(\tilde{G}(z_t))^\top \left(J_{\tilde{g}_\phi}(\tilde{G}(z(s))) J_{\tilde{G}}(z(s)) - J_{\tilde{g}_\phi}(\tilde{G}(z_t)) J_{\tilde{G}}(z_t) \right) ds \right\|_2 \leq \quad (16)$$

$$\int_0^1 \|J_{\tilde{G}}(z_t)\|_2 \|J_{\tilde{g}_\phi}(\tilde{G}(z_t))\|_2 \left\| J_{\tilde{g}_\phi}(\tilde{G}(z(s))) J_{\tilde{G}}(z(s)) - J_{\tilde{g}_\phi}(\tilde{G}(z_t)) J_{\tilde{G}}(z_t) \right\|_2 ds. \quad (17)$$

Combining (15)–(17) yields

$$\begin{aligned} \|\mathcal{T}_t\|_2 &\leq \left\| I - 2\lambda J_{\tilde{G}}(z_t)^\top J_{\tilde{g}_\phi}(\tilde{G}(z_t))^\top J_{\tilde{g}_\phi}(\tilde{G}(z_t)) J_{\tilde{G}}(z_t) \right\|_2 \|z_t - z^*\|_2 \\ &\quad + 2\lambda \left(\int_0^1 \|J_{\tilde{G}}(z_t)\|_2 \|J_{\tilde{g}_\phi}(\tilde{G}(z_t))\|_2 \left\| J_{\tilde{g}_\phi}(\tilde{G}(z(s))) J_{\tilde{G}}(z(s)) - J_{\tilde{g}_\phi}(\tilde{G}(z_t)) J_{\tilde{G}}(z_t) \right\|_2 ds \right) \|z_t - z^*\|_2. \end{aligned} \quad (18)$$

We bound the difference inside the integral by writing

$$\begin{aligned} &\left\| J_{\tilde{g}_\phi}(\tilde{G}(z(s))) J_{\tilde{G}}(z(s)) - J_{\tilde{g}_\phi}(\tilde{G}(z_t)) J_{\tilde{G}}(z_t) \right\|_2 \\ &\leq \left\| (J_{\tilde{g}_\phi}(\tilde{G}(z(s))) - J_{\tilde{g}_\phi}(\tilde{G}(z_t))) J_{\tilde{G}}(z(s)) \right\|_2 + \left\| J_{\tilde{g}_\phi}(\tilde{G}(z_t)) (J_{\tilde{G}}(z(s)) - J_{\tilde{G}}(z_t)) \right\|_2 \\ &\leq \|J_{\tilde{g}_\phi}(\tilde{G}(z(s))) - J_{\tilde{g}_\phi}(\tilde{G}(z_t))\|_2 \|J_{\tilde{G}}(z(s))\|_2 + \|J_{\tilde{g}_\phi}(\tilde{G}(z_t))\|_2 \|J_{\tilde{G}}(z(s)) - J_{\tilde{G}}(z_t)\|_2. \end{aligned} \quad (19)$$

Using the Lipschitz property of $J_{\tilde{G}}$,

$$\|J_{\tilde{G}}(z(s)) - J_{\tilde{G}}(z_t)\|_2 \leq L_G \|z(s) - z_t\|_2 = L_G(1-s) \|z_t - z^*\|_2,$$

together with the Lipschitz continuity of $J_{\tilde{g}_\phi}$,

$$\|J_{\tilde{g}_\phi}(\tilde{G}(z(s))) - J_{\tilde{g}_\phi}(\tilde{G}(z_t))\|_2 \leq L_\phi M_G(1-s) \|z_t - z^*\|_2,$$

and the uniform bounds

$$\|J_{\tilde{G}}(z(s))\|_2 \leq M_G, \quad \|J_{\tilde{g}_\phi}(\tilde{G}(z_t))\|_2 \leq M_\phi,$$

This yields

$$\left\| J_{\tilde{g}_\phi}(\tilde{G}(z(s))) J_{\tilde{G}}(z(s)) - J_{\tilde{g}_\phi}(\tilde{G}(z_t)) J_{\tilde{G}}(z_t) \right\|_2 \leq (1-s) \left(L_\phi M_G^2 + L_G M_\phi \right) \|z_t - z^*\|_2.$$

Substituting this bound into (18) and integrating over $s \in [0, 1]$ yields

$$\begin{aligned} \|\mathcal{T}_t\|_2 &\leq \left\| I - 2\lambda J_{\tilde{G}}(z_t)^\top J_{\tilde{g}_\phi}(\tilde{G}(z_t))^\top J_{\tilde{g}_\phi}(\tilde{G}(z_t)) J_{\tilde{G}}(z_t) \right\|_2 \|z_t - z^*\|_2 \\ &\quad + \lambda \left(L_\phi M_G^3 M_\phi + L_G M_\phi^2 M_G \right) \|z_t - z^*\|_2^2. \end{aligned} \quad (20)$$

Since the symmetric matrix

$$S_t := J_{\tilde{G}}(z_t)^\top J_{\tilde{g}_\phi}(\tilde{G}(z_t))^\top J_{\tilde{g}_\phi}(\tilde{G}(z_t)) J_{\tilde{G}}(z_t)$$

has eigenvalues contained in $[m_G^2 m_\phi^2, M_G^2 M_\phi^2]$, its spectral norm satisfies

$$\|I - 2\lambda S_t\|_2 = \max_{\sigma \in [m_G^2 m_\phi^2, M_G^2 M_\phi^2]} |1 - 2\lambda\sigma|.$$

For any $0 < \lambda \leq 1/(2M_G^2 M_\phi^2)$, the maximum is attained at $\sigma = m_G^2 m_\phi^2$, and hence

$$\|I - 2\lambda S_t\|_2 \leq 1 - 2\lambda m_G^2 m_\phi^2.$$

Substituting this bound into (20) yields

$$\|\mathcal{T}_t\|_2 \leq \left(1 - 2\lambda m_G^2 m_\phi^2 + \lambda \left(L_\phi L_G M_G^2 M_\phi + L_G M_\phi^2 M_G \right) \|z_t - z^*\|_2 \right) \|z_t - z^*\|_2. \quad (21)$$

Therefore, if

$$\|z_t - z^*\|_2 < \frac{2m_G^2 m_\phi^2}{L_\phi M_G^3 M_\phi + L_G M_\phi^2 M_G} \quad \text{and} \quad 0 < \lambda \leq \frac{1}{2M_G^2 M_\phi^2},$$

then the contractive part satisfies the strict contraction

$$\|\mathcal{T}_t\|_2 \leq (1 - 2\lambda m_G^2 m_\phi^2) \|z_t - z^*\|_2,$$

with contraction factor strictly smaller than one. By the definitions of the approximation and misalignment errors,

$$\|\tilde{f}(\bar{x}) - \tilde{f}(x)\|_2 = \sqrt{N} \sqrt{\text{ApproxErr}(x, \bar{x})}, \quad \|\tilde{f}(x) - \tilde{g}_\phi(\tilde{G}(z^*))\|_2 = \sqrt{N} \sqrt{\text{MisREPA}(x)}.$$

Returning to the decomposition we combine the contraction bound for \mathcal{T}_t with the remaining two terms. Using the triangle inequality together with the uniform bounds $\|J_{\tilde{G}}(z_t)\|_2 \leq M_G$ and $\|J_{\tilde{g}_\phi}(\tilde{G}(z_t))\|_2 \leq M_\phi$, we obtain

$$\begin{aligned} \|z_t^{(\text{repa})} - z^*\|_2 &\leq \|\mathcal{T}_t\|_2 + 2\lambda M_G M_\phi \|\tilde{f}(\bar{x}) - \tilde{f}(x)\|_2 \\ &\quad + 2\lambda M_G M_\phi \|\tilde{f}(x) - \tilde{g}_\phi(\tilde{G}(z^*))\|_2. \end{aligned} \quad (22)$$

Substituting the contraction estimate together with the above identities yields

$$\|z_t^{(\text{REPA})} - z^*\|_2 \leq (1 - \lambda m_J m_\phi) \|z_t - z^*\|_2 + C \left(\sqrt{\text{ApproxErr}(x, \bar{x})} + \sqrt{\text{MisREPA}(x)} \right), \quad (23)$$

where the constant C is defined explicitly as

$$C := 2\lambda M_G M_\phi.$$

This concludes the proof.

A.2. Details About Latent DPS + REPA Implementation

We implement Latent DPS + REPA following Algorithm 2 and use 1000 sampling steps throughout. We employ an SNR-based learning rate schedule of the form

$$\eta(t) = \frac{\kappa}{\max\left(\frac{t}{1-t}, 1\right)},$$

where κ is a tunable scaling factor. This schedule accounts for the varying signal-to-noise ratio across diffusion timesteps and provides stable performance in practice. The parameters κ and the representation-alignment strength λ are tuned on a small validation set with present the best parameters found in Table 2.

Table 2. Hyperparameters used for Latent DPS + REPA. ImageNet uses Gaussian noise $\sigma = 0.01$, while FFHQ uses $\sigma = 0.05$.

| Task | ImageNet | | FFHQ | |
|---------------------|----------|-----------|----------|-----------|
| | κ | λ | κ | λ |
| Super-resolution | 2.0 | 0.01 | 0.025 | 1.25 |
| Gaussian deblurring | 0.25 | 0.05 | 0.05 | 0.5 |
| Motion deblurring | 0.5 | 0.01 | 0.05 | 0.5 |
| Box inpainting | 0.5 | 0.01 | 0.025 | 0.75 |

Algorithm 2 Latent DPS + REPA Algorithm

Require: flow model u_θ , measurement y , pretrained encoder f , proxy representation c_{proxy} , timestep t_{cutoff}

- 1: initialize $x_T \sim \mathcal{N}(0, I)$
- 2: **for** $t \in \{T, \dots, 0\}$ **do**
- 3: $v \leftarrow u_\theta(z_t, t)$
- 4: $\hat{z}_0 \leftarrow \mathbb{E}[z_0 \mid z_t]$
- 5: $\Delta t \leftarrow 1/T$
- 6: $z_{t-1} \leftarrow z_t - \Delta t \cdot v$
- 7: $z_{t-1} \leftarrow z_{t-1} - \eta \nabla_{z_t} \|y - \mathcal{A}(\mathcal{D}(\hat{z}_0))\|_2^2$
- 8: $z_{t-1} \leftarrow z_{t-1} + \lambda \nabla_{z_t} \sum_{n=1}^N \cos(c_{\text{proxy}}^{[n]}, g_\phi(\text{DiffEnc}^{[n]}(z_t, t)))$
- 9: **if** $t < t_{\text{cutoff}}$ **then**
- 10: $c_{\text{proxy}} \leftarrow f_{\text{DINOv2}}(\mathcal{D}(\mathbb{E}[z_0 \mid z_t]))$
- 11: **end if**
- 12: **end for**
- 13: **return** x_0

A.3. Details About Resample + REPA Implementation

In Table 3, we present an adaptation of the algorithm proposed by Song et al. (2024) to the flow-based setting, augmented with the REPA regularizer as described in the methodology section. We note that the original ReSample algorithm employs a three-stage procedure for enforcing data consistency: (i) gradient steps in latent space, similar to Latent DPS; (ii) pixel-space optimization, which is computationally efficient and captures high-level semantics but often leads to blurrier reconstructions; and (iii) latent space optimization as outlined to line 7 of Algorithm 3. In contrast, our adaptation omits the pixel-space stage, as our focus is on maximizing perceptual quality. We found that this modification together with the inclusion of the REPA regularizer yields sharper and more visually convincing results, while still benefiting from the refinement effect of the final latent-space consistency updates. The best hyperparameters used for this variant are reported in Table 3. In addition to the parameters κ and λ , which play analogous roles to those in Latent DPS, we also tune the maximum number of inner-loop optimization steps and the corresponding inner learning rate of the Resample procedure (see Algorithm 3).

A.4. Robustness of DINOv2 Representations to Corruptions

To evaluate the robustness of DINOv2 representations under various corruptions, we conduct experiments on a fixed set of 100 images. For each image, we compute the average patch similarity between its ground truth representation and that of its corrupted version. We assess this similarity across different corruption types specifically super-resolution and Gaussian deblurring at varying levels of severity. We report the average similarity across the selected subset of 100 images.

Figure 4 presents how DINOv2 representation similarity changes as the corruption severity increases for the two tasks. Figure 5 further visualizes how the pixel-space appearance of a single image changes across corruption levels. Interestingly, we observe that DINOv2 representations remain significantly more robust to both super-resolution and Gaussian deblurring. Despite substantial visual degradation in pixel space, DINOv2 features maintain a strong alignment with the original image features.

Table 3. Hyperparameters used for Resampling + REPA. ImageNet uses Gaussian noise $\sigma = 0.01$, while FFHQ uses $\sigma = 0.05$.

| Task | ImageNet | | | | FFHQ | | | |
|---------------------|----------|-----------|-----------|----------|----------|-----------|-----------|----------|
| | κ | λ | max iters | inner lr | κ | λ | max iters | inner lr |
| Super-resolution | 0.05 | 3.25 | 150 | 0.005 | 0.01 | 2.25 | 100 | 0.0001 |
| Gaussian deblurring | 0.075 | 0.5 | 300 | 0.005 | 0.05 | 0.75 | 300 | 0.00075 |
| Motion deblurring | 0.5 | 0.75 | 300 | 0.005 | 0.05 | 0.75 | 100 | 0.005 |
| Box inpainting | 0.025 | 100 | 200 | 0.0005 | 0.05 | 0.75 | 200 | 0.0005 |

Algorithm 3 Resample + REPA Algorithm

Require: flow model u_θ , measurement y , pretrained encoder f , resample steps C , parameter γ , proxy representation c_{proxy} , timestep t_{cutoff}

- 1: initialize $z_T \sim \mathcal{N}(0, I)$
- 2: **for** $t \in \{T, \dots, 0\}$ **do**
- 3: $v \leftarrow u_\theta(z_t, t)$
- 4: $\hat{z}_0 \leftarrow \mathbb{E}[z_0 | z_t]$
- 5: $\Delta t \leftarrow 1/T$
- 6: $z_{t-1} \leftarrow z_t - \Delta t \cdot v$
- 7: **if** $t \in C$ **then**
- 8: $\tilde{z}_0(y) \leftarrow \arg \min_z \frac{1}{2} \|y - \mathcal{A}(\mathcal{D}(z))\|_2^2$ ▷ initialize at \hat{z}_0
- 9: $z_{t-1} \leftarrow \text{STOCHASTICRESAMPLE}(\tilde{z}_0(y), z_{t-1}, \gamma)$
- 10: **end if**
- 11: $z_{t-1} \leftarrow z_{t-1} - \eta \nabla_{z_t} \|y - \mathcal{A}(\mathcal{D}(\hat{z}_0))\|_2^2$
- 12: $z_{t-1} \leftarrow z_{t-1} + \lambda \nabla_{z_t} \sum_{n=1}^N \cos(c_{\text{proxy}}^{[n]}, g_\phi(\text{DiffEnc}^{[n]}(z_t, t)))$
- 13: **if** $t < t_{\text{cutoff}}$ **then**
- 14: $c_{\text{proxy}} \leftarrow f_{\text{DINOv2}}(\mathcal{D}(\mathbb{E}[z_0 | z_t]))$
- 15: **end if**
- 16: **end for**
- 17: $x_0 \leftarrow \mathcal{D}(z_0)$
- 18: **return** x_0

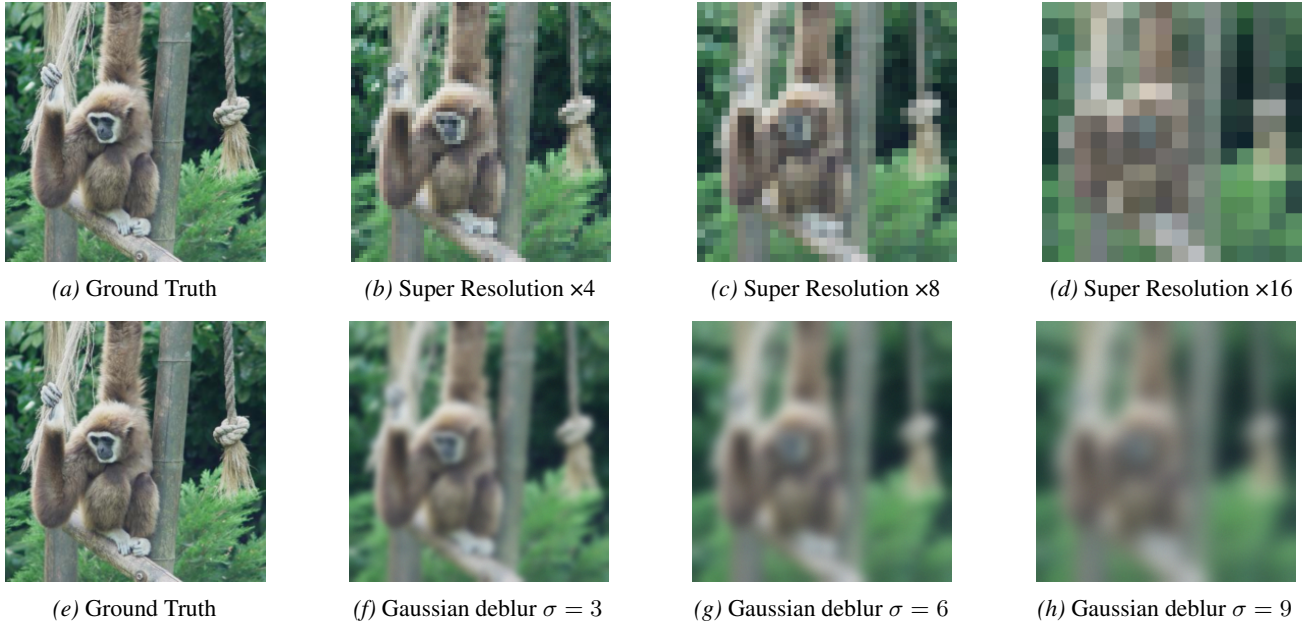


Figure 5. Visual comparison of a corrupted image used in the similarity experiments for different corruption types and severity levels.

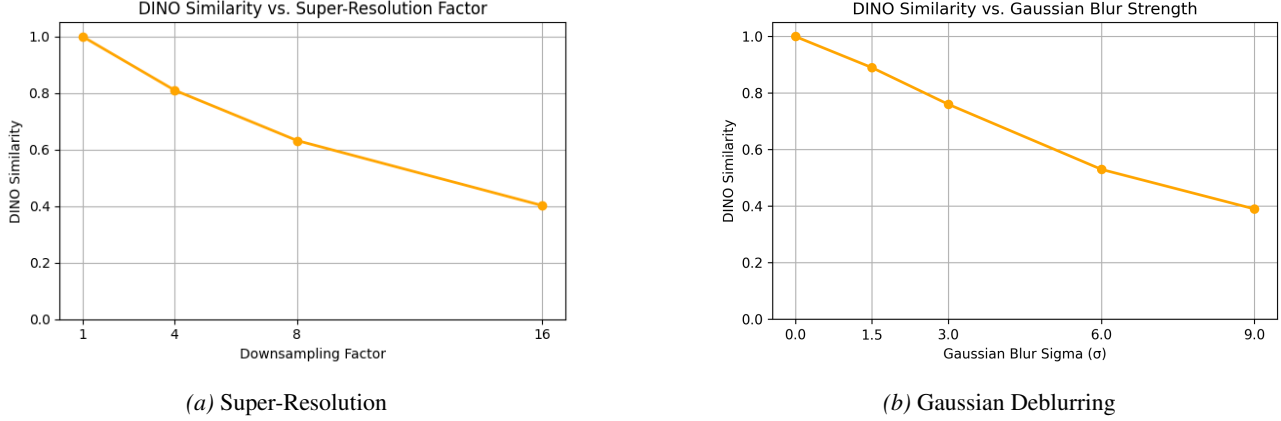


Figure 4. Similarity of representations under increasing levels of corruption.

A.5. Selection of Proxy Representation

Since pretrained DINOv2 features are robust to a wide range of common image corruptions, we use the DINOv2 encoding of the measurement as an initial proxy representation, $f_{\text{DINOv2}}(y)$. We find this choice to be effective across all considered inverse problems. In addition, we introduce a cutoff timestep at which the proxy representation is updated to depend on the model’s current denoised estimate, namely $f_{\text{DINOv2}}(\mathcal{D}(\mathbb{E}[z_0 | z_t]))$.

- **Box Inpainting.** We construct the proxy representation by combining the observed regions of the measurement with the model’s current denoised estimate:

$$c_{\text{proxy}} = \text{mask} \odot f_{\text{DINOv2}}(y) + (I - \text{mask}) \odot f_{\text{DINOv2}}(\mathcal{D}(\mathbb{E}[z_0 | z_t])), \quad (24)$$

where mask denotes the binary inpainting mask.

- **Super-resolution, Gaussian Deblurring, and Motion Deblurring.** For these tasks, we use $f_{\text{DINOv2}}(y)$ as the proxy representation during the early stages of sampling. On the FFHQ dataset, we find it beneficial to switch to the reconstruction-based proxy $f_{\text{DINOv2}}(\mathcal{D}(\mathbb{E}[z_0 | z_t]))$ after 80% of the diffusion steps. On ImageNet, this transition yields only marginal improvements, and we therefore use the measurement-based proxy throughout.

A.6. Experimental Details

We implement the inverse problem operators following the setups of Chung et al. (2023). For deblurring tasks, we follow Zhang et al. (2025) and fix a single realization of the degradation operator to ensure fair and consistent comparisons across methods. All baseline results are obtained using the official implementations provided by Chung et al. (2023) and Zhang et al. (2025).

For DPS, we use the dataset-specific hyperparameters reported in the original paper. For DAPS, we adopt the hyperparameters provided in the official codebase for latent diffusion models. For PSNR and SSIM, we report results obtained by averaging the reconstructed images across five independent runs of the solver and then computing the metrics on the averaged reconstruction.

A.7. Enforcing Feature-Level DINOv2 Consistency without Representation Alignment

In this ablation study, we compare REPA against a variant that enforces consistency directly in the DINOv2 feature-space, without involving the diffusion model representations. More specifically, instead of using the representation alignment loss in line 8 of Algorithm 2, we replace it with the following update step:

$$z_{t-1} \leftarrow z_{t-1} + \lambda \nabla_{z_t} \sum_{n=1}^N \cos \left(c_{\text{proxy}}^{[n]}, f_{\text{DINOv2}}^{[n]}(\mathcal{D}(\mathbb{E}[z_0 | z_t])) \right), \quad (25)$$

Note that in this case we can only use $f_{\text{DINOv2}}(y)$ as the proxy term. While both objectives influence the sampling trajectory, the feature-only variant derives its guidance from the DINOv2 features of the decoded image. In contrast, REPA aligns the diffusion model’s internal representations with DINOv2 features directly at each timestep.

As shown in Table 4, the direct feature-space alignment yields consistently lower perceptual quality than the proposed representation-based formulation. For both experiments we have chosen the best hyperparameters using a small grid search as in A.2 to ensure fairness in comparison. Figure 6 further illustrates this difference: REPA reconstructions are sharper and more faithful to the ground truth for both super-resolution and Gaussian deblurring. These results demonstrate that aligning the diffusion model’s internal representations provides a stronger and more semantically guided inductive bias than feature-space matching alone.

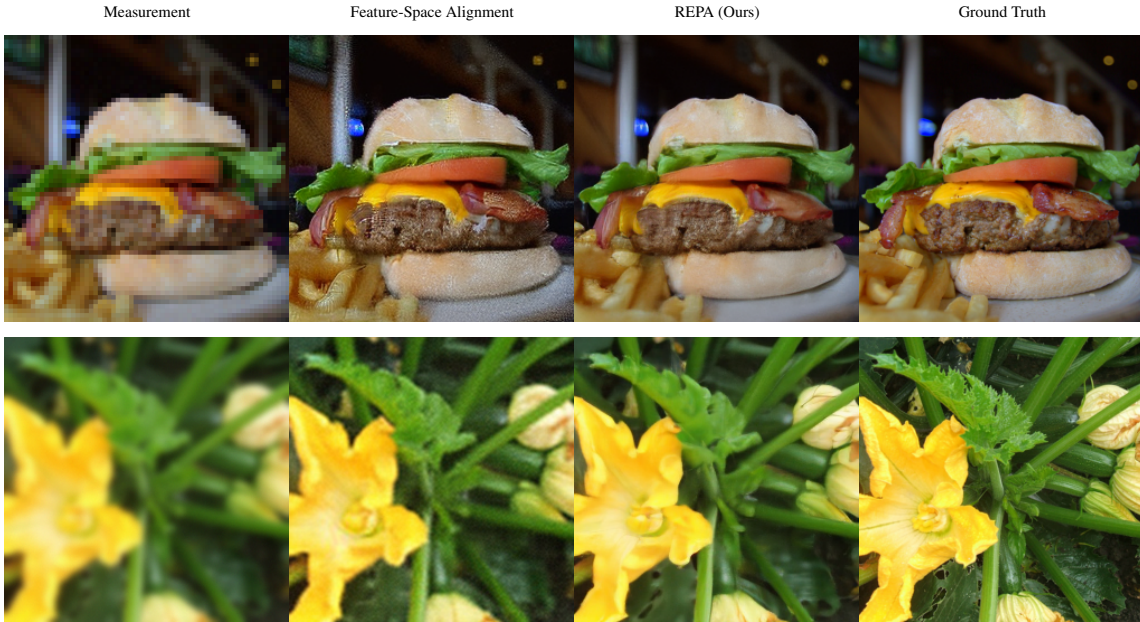


Figure 6. **Qualitative comparison between feature-space and representation-space alignment.** Results are shown for super-resolution (top row) and Gaussian deblurring.

Table 4. Quantitative comparison between REPA and direct feature-space alignment. LPIPS and FID results for super-resolution and Gaussian deblurring on the ImageNet validation set. Qualitative examples for the same tasks are shown in Figure 6.

| Method | Super-resolution ($\times 4$) | | Gaussian deblurring | |
|-------------------------------------|---------------------------------|------------------|---------------------|------------------|
| | LPIPS \downarrow | FID \downarrow | LPIPS \downarrow | FID \downarrow |
| Feature-space alignment | 0.227 | 95.69 | 0.276 | 128.29 |
| Representation alignment (proposed) | 0.217 | 86.88 | 0.256 | 102.99 |

A.8. Representation Alignment on an Independently Pretrained Model

The effectiveness of REPA for inverse problems relies on the availability of a mapping g_ϕ between the internal representations of the diffusion model and the DINOv2 feature space. Such a mapping is naturally available when the diffusion model is pretrained with representation alignment. However, when starting from a diffusion model that has been pretrained independently, this alignment is not present.

To construct the mapping g_ϕ , we finetune the pretrained diffusion model using the representation alignment objective introduced in Eq. 6. However, optimizing the REPA objective in isolation can cause the diffusion model to drift away from the natural image manifold, degrading its denoising and generative performance. To prevent this drift and preserve the learned image prior, we jointly optimize the standard velocity prediction objective $\mathcal{L}_{\text{velocity}}$ (Eq. 3). The resulting finetuning objective is

$$\mathcal{L}_{\text{finetune}} := -\text{REPA}(x, h_t) + \lambda \mathcal{L}_{\text{velocity}}, \quad (26)$$

Table 5. Performance comparison on FFHQ ($\sigma = 0.05$) for models trained and finetuned with REPA. Lower is better for LPIPS/FID, higher is better for PSNR/SSIM. Best values per task are shown in **bold**.

| Task | Method | LPIPS↓ | FID↓ | PSNR↑ | SSIM↑ |
|-----------------|-----------------------------------|--------------|--------------|--------------|--------------|
| 4× SR | Latent DPS (REPA model) | 0.188 | 56.69 | 28.99 | 0.814 |
| | Latent DPS + REPA (REPA model) | 0.177 | 51.27 | 29.12 | 0.819 |
| | Latent DPS (SiT) | 0.190 | 61.36 | 28.92 | 0.805 |
| | Latent DPS + REPA (SiT finetuned) | 0.184 | 59.22 | 28.95 | 0.805 |
| Gaussian Deblur | Latent DPS (REPA model) | 0.192 | 60.65 | 28.15 | 0.783 |
| | Latent DPS + REPA (REPA model) | 0.186 | 55.53 | 28.21 | 0.787 |
| | Latent DPS (SiT) | 0.193 | 60.72 | 28.02 | 0.782 |
| | Latent DPS + REPA (SiT finetuned) | 0.188 | 59.76 | 28.07 | 0.779 |
| Motion Deblur | Latent DPS (REPA model) | 0.170 | 52.14 | 27.20 | 0.773 |
| | Latent DPS + REPA (REPA model) | 0.165 | 47.18 | 27.16 | 0.772 |
| | Latent DPS (SiT) | 0.171 | 54.01 | 27.63 | 0.779 |
| | Latent DPS + REPA (SiT finetuned) | 0.167 | 52.45 | 27.75 | 0.780 |

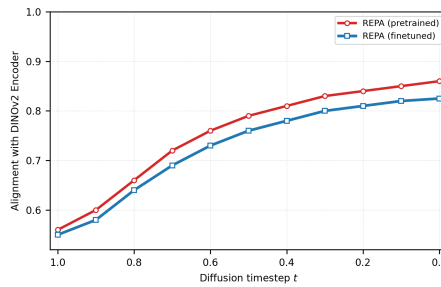


Figure 7. Cosine alignment between internal diffusion representations and DINOv2 encoder across diffusion timesteps.

where x denotes a clean input image, h_t denotes the corresponding internal diffusion representation at noise level t , extracted from a fixed intermediate layer of the pretrained diffusion model as defined in 2.2. We set $\lambda = 1$ in all experiments.

We evaluate this finetuning strategy on the FFHQ dataset. Specifically, we first train an SiT model without representation alignment for 100k iterations and subsequently perform full finetuning of the model for an additional 20k iterations using the combined objective above to learn the alignment mapping g_ϕ . We then apply REPA to inverse problems using the finetuned model. Table 5 reports the corresponding results, alongside those obtained with a model pretrained with representation alignment.

Across all inverse problems, adding REPA consistently improves perceptual metrics (LPIPS and FID), demonstrating that finetuning with the proposed alignment objective is sufficient to enable effective use of REPA at inference time. While the strongest gains are obtained when the diffusion model is pretrained with representation alignment, the finetuned model exhibits the same qualitative behavior, indicating that alignment can be introduced post hoc without retraining the diffusion model from scratch.

To examine this behavior more closely, we conduct the following analysis. We select a subset of 1000 images from the FFHQ validation set and measure the cosine alignment between the internal representations of the diffusion model and those of the DINOv2 encoder across diffusion timesteps. Figure 7 shows that, although finetuning successfully learns a meaningful alignment mapping, the model pretrained with representation alignment consistently achieves higher alignment values throughout the denoising trajectory. In terms of Definition 4.1, this corresponds to a smaller MisREPA error, explaining why REPA provides more accurate regularization signals for inverse problems when applied to an alignment-pretrained model.

A.9. Additional Qualitative Results

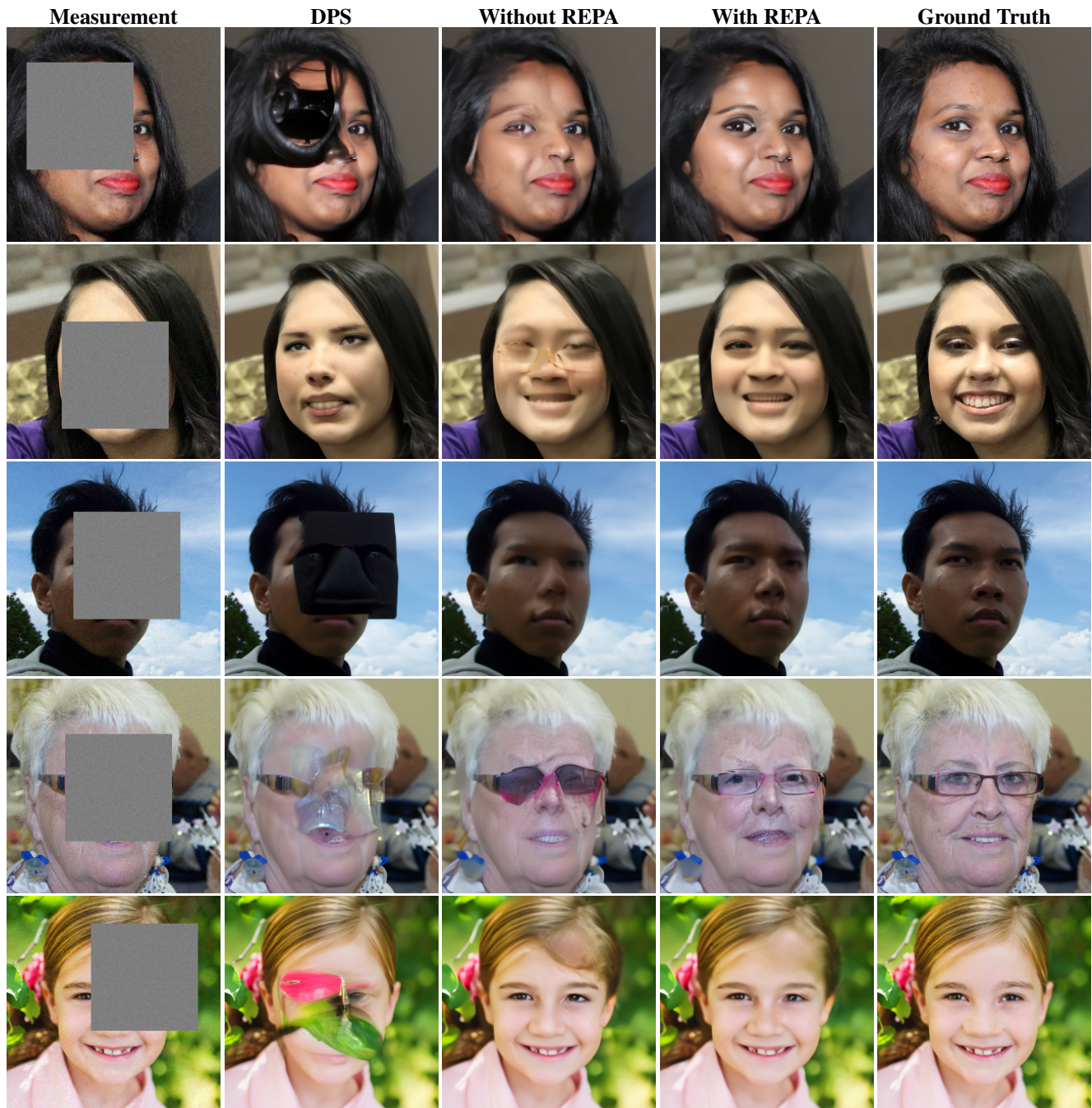


Figure 8. Qualitative comparison for box inpainting on the FFHQ dataset. Each row shows (from left to right): the measurement, the baseline method (DPS), the baseline latent solver (Latent DPS or ReSample), its REPA-enhanced variant, and the ground truth. The first two rows correspond to ReSample, while the last two correspond to Latent DPS.

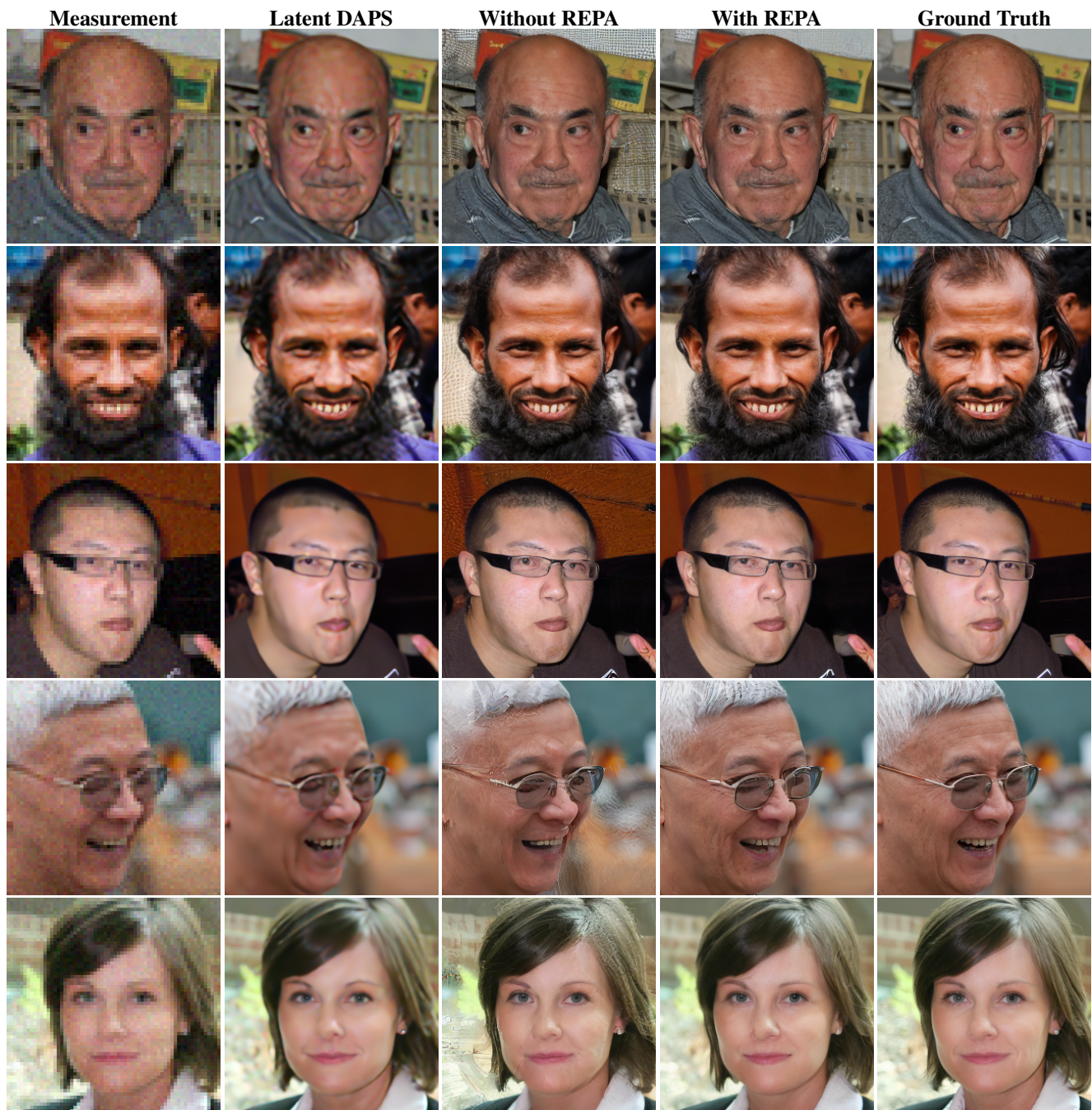


Figure 9. Qualitative comparison for $4\times$ super-resolution on the FFHQ dataset. Each row shows (from left to right): the measurement, the baseline method (Latent DAPS), the baseline latent solver (Latent DPS or ReSample), its REPA-enhanced variant, and the ground truth. The first two rows correspond to ReSample, while the last three correspond to Latent DPS.

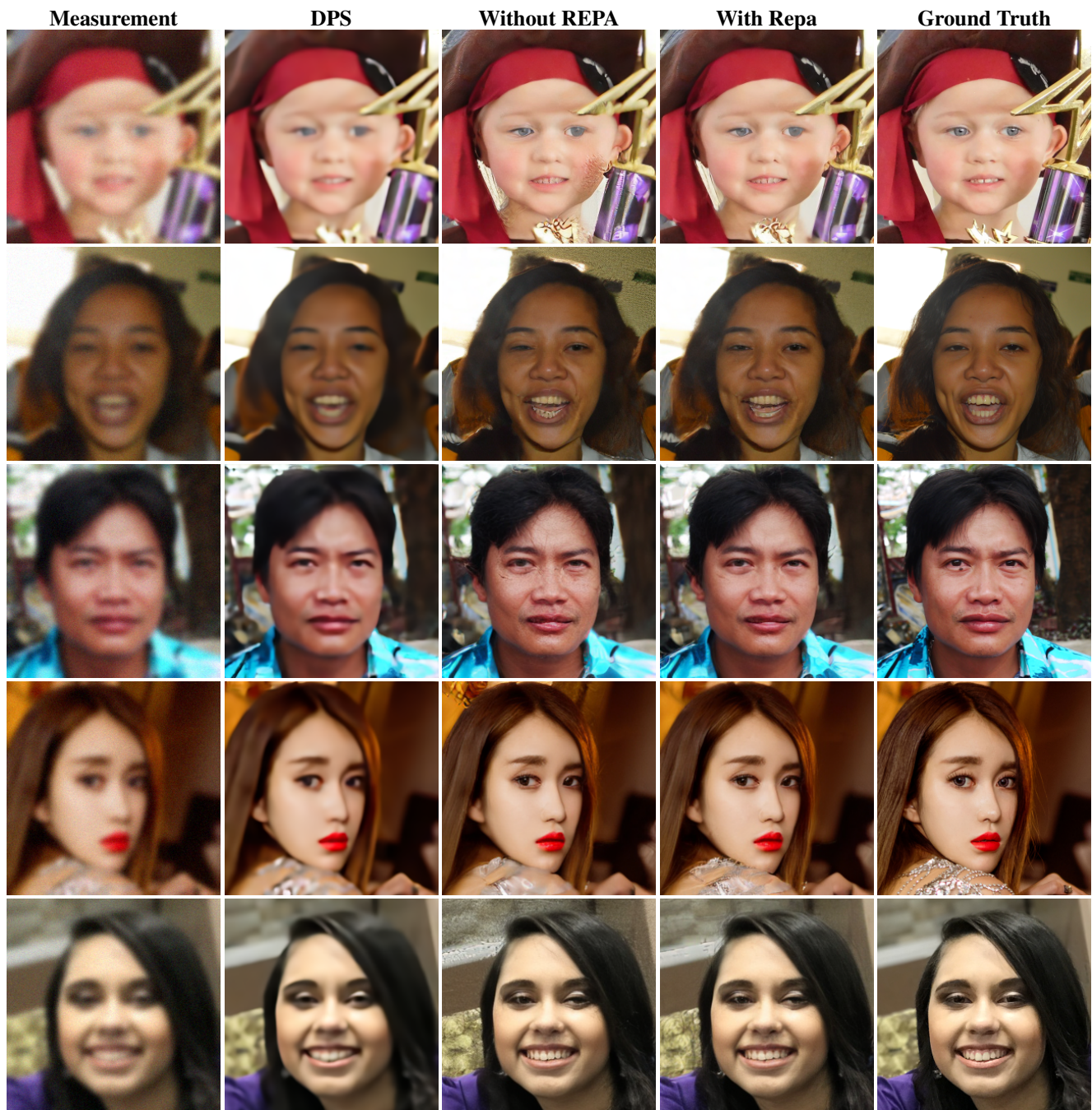


Figure 10. Qualitative comparison for Gaussian Deblurring on the FFHQ dataset. Each row shows (from left to right): the measurement, the baseline method (Latent DAPS), the baseline latent solver (Latent DPS or ReSample), its REPA-enhanced variant, and the ground truth. The first two rows correspond to ReSample, while the last three correspond to Latent DPS.



Figure 11. Qualitative comparison for Motion Deblurring on the FFHQ dataset. Each row shows (from left to right): the measurement, the baseline method (DPS), the baseline latent solver (Latent DPS or ReSample), its REPA-enhanced variant, and the ground truth. The first two rows correspond to ReSample, while the last three correspond to Latent DPS.

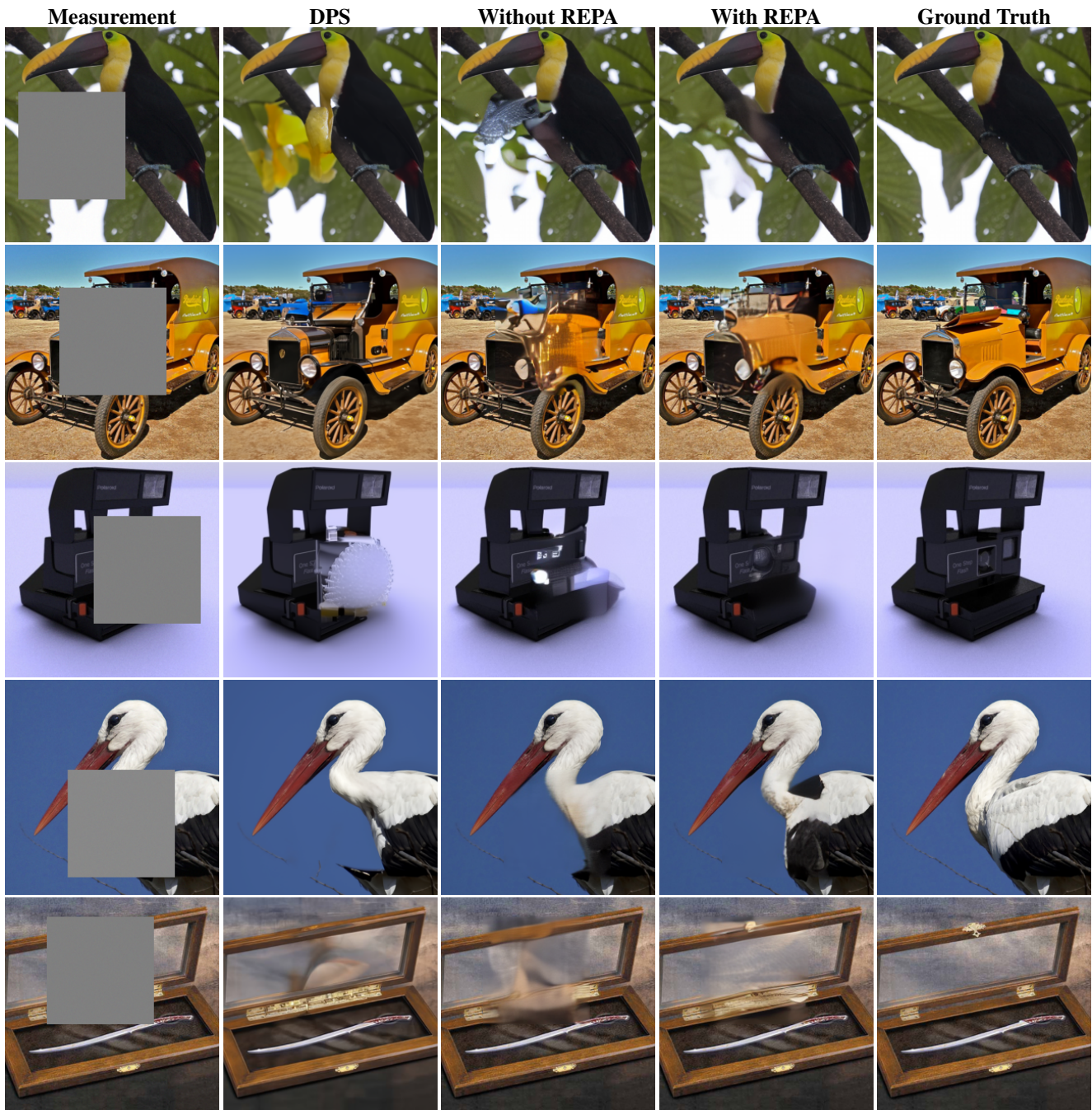


Figure 12. Qualitative comparison for box inpainting on the ImageNet dataset. Each row shows (from left to right): the measurement, the baseline method (DPS), the baseline latent solver (Latent DPS or ReSample), its REPA-enhanced variant, and the ground truth. The first three rows correspond to ReSample, while the last two correspond to Latent DPS.

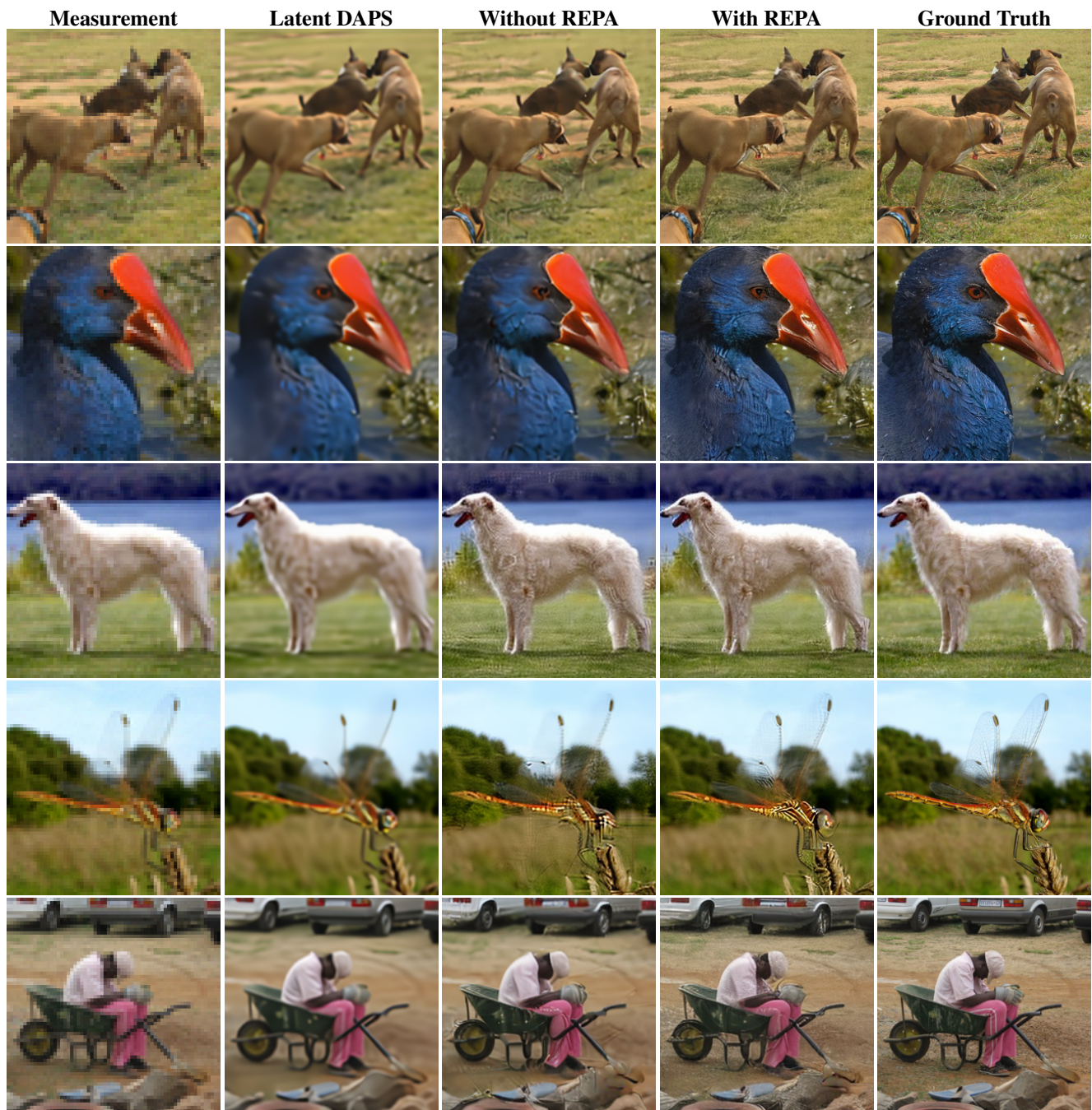


Figure 13. Qualitative comparison for Super resolution on the ImageNet dataset. Each row shows (from left to right): the measurement, the baseline method (Latent DAPS), the baseline latent solver (Latent DPS or ReSample), its REPA-enhanced variant, and the ground truth. The first three rows correspond to ReSample, while the last two correspond to Latent DPS.

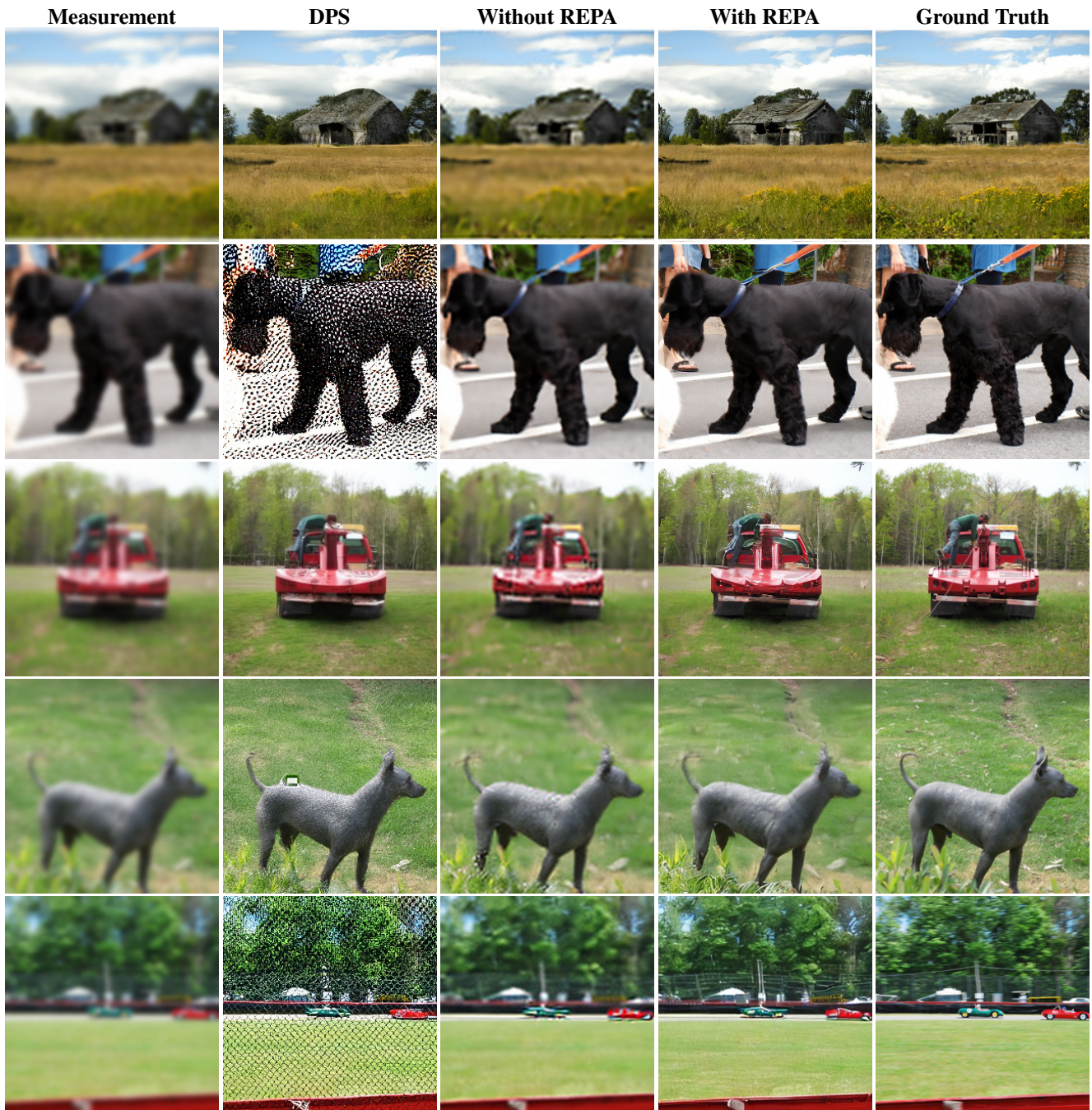


Figure 14. Qualitative comparison for Gaussian Deblurring on the ImageNet dataset. Each row shows (from left to right): the measurement, the baseline method (DPS), the baseline latent solver (Latent DPS or ReSample), its REPA-enhanced variant, and the ground truth. The first three rows correspond to ReSample, while the last two correspond to Latent DPS.

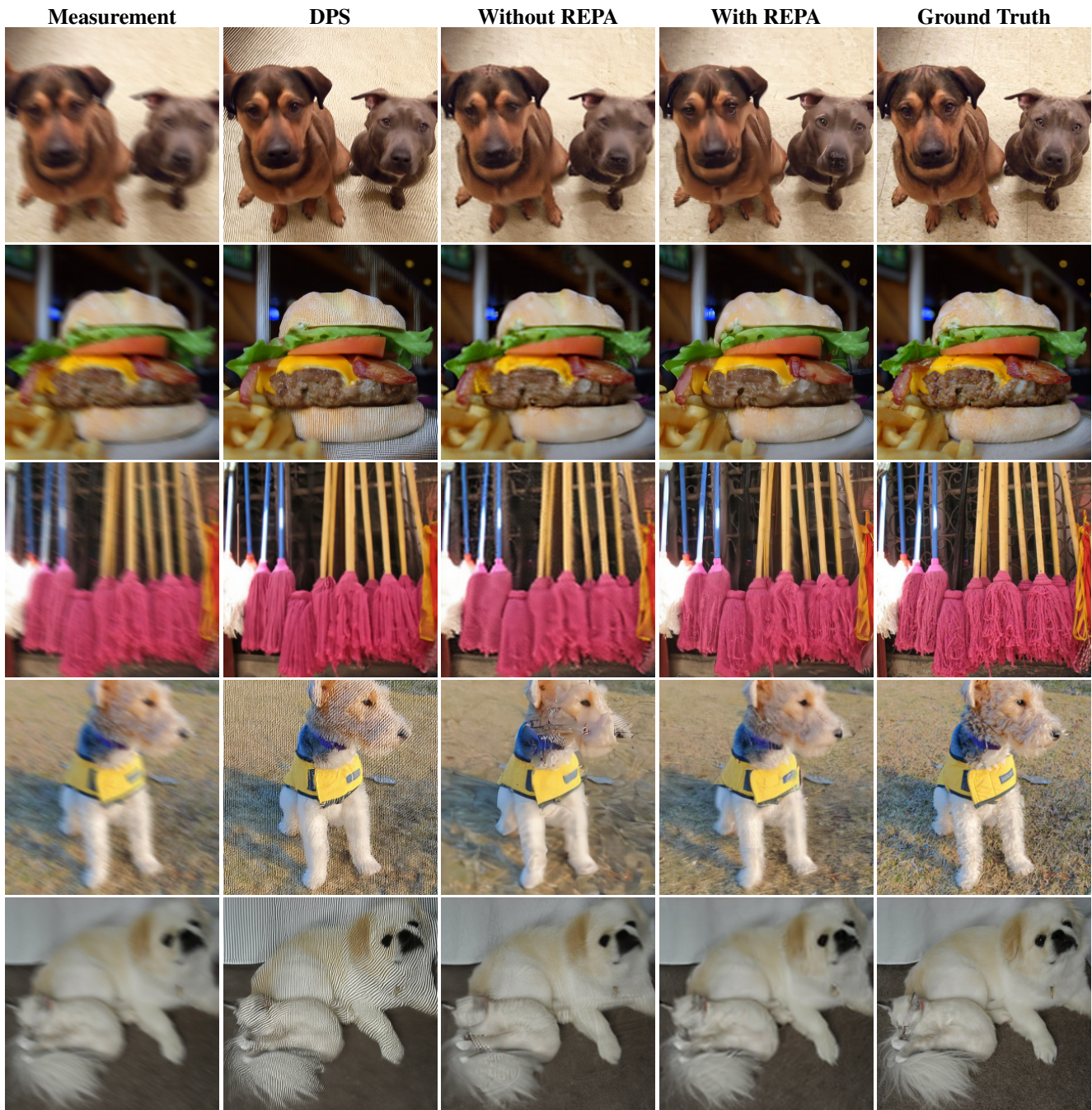


Figure 15. Qualitative comparison for Motion Deblurring on the ImageNet dataset. Each row shows (from left to right): the measurement, the baseline method (DPS), the baseline latent solver (Latent DPS or ReSample), its REPA-enhanced variant, and the ground truth. The first three rows correspond to ReSample, while the last two correspond to Latent DPS.